Chinese Journal of Chemical Engineering 95 (2026) 328–346

Contents lists available at ScienceDirect

Chinese Journal of Chemical Engineering

journal homepage: www.elsevier.com/locate/CJChE

Full Length Article

Bubble distribution and mass transfer by experiments and flow field characteristics by CFD simulation in a self-rotating hydraulic stirring tank driven with multi-nozzle jets

Denghan Luo [1], Xiaopeng Chen [1], Zhongyao Zhang [1], Yong Jin [2], Jiezhen Liang [1], Zhangfa Tong [1], Linlin Wang [1, *]

[1] School of Chemistry and Chemical Engineering, Guangxi Key Laboratory of Petrochemical Resource Processing and Process Intensification Technology, Guangxi University, Nanning 530004, China
[2] Guangxi Huayi Energy Chemical Co., Ltd., Qinzhou 535000, China

ARTICLE INFO

Article history:
Received 7 January 2026
Received in revised form
5 March 2026
Accepted 10 March 2026
Available online 20 April 2026

Keywords:
Hydraulic agitator
Bubble distribution
Gas–liquid mass transfer
Flow field characteristics
CFD simulations

ABSTRACT

Gas–liquid mixing and mass transfer in jet-driven tanks are crucial for multiphase systems. However, the understanding of these devices remains limited. Herein, a novel self-rotating hydraulic agitator with a semi-circular, multi-nozzle, and multi-layer jet design was integrated into a tank. High-speed imaging and dynamic gassing-in were used to characterize the bubbles and measure the volumetric mass transfer coefficient (k_La). The hydraulic stirring tank generated self-rotating vortices and strong shear forces, promoting bubble break-up compared to a mechanical stirring tank, reducing the Sauter mean diameter (d_{32}) by 25%–40%, increasing the deformation rate ($\bar{E}$) by 7%–8%, and enhancing k_La by 20%–45%. Higher gas and liquid rates intensified the flow disturbances and gas–liquid contact. Appropriate baffles suppress circulation and vortex cores while enhancing local turbulence. The counter-directional configuration of the hydraulic agitator and gas distributor enhanced radial flow and shear interactions, generating smaller, more spherical bubbles that decreased d_{32} by 4%–8%, increased the $\bar{E}$ by 4%–5.5%, and improved k_La by 3%–11%. The effect of pulsed intake mode on gas–liquid mass transfer was investigated, and no observable enhancement was observed under the tested conditions. Computational fluid dynamics (CFD) simulations were conducted to investigate the flow field and turbulence interaction. These findings reveal that the mechanisms enhancing tank performance include self-rotating vortices, high-velocity shear, multi-zone flow coupling, and gas–liquid interactions, thereby providing valuable insights for optimizing both the tank structure and agitator design of fluid-jet-driven apparatuses.
© 2026 The Chemical Industry and Engineering Society of China, and Chemical Industry Press Co., Ltd. All rights are reserved, including those for text and data mining, AI training, and similar technologies.

1. Introduction

Multiphase mixing is an indispensable unit operation in petrochemical, fine chemical, biological fermentation, and energy conversion processes [1–3]. The bubble distribution, gas–liquid mass transfer, and flow field characteristics in multiphase tanks determine their overall mixing performance [4–6]. Despite their widespread application, traditional mechanical stirring tanks, as conventional mixing enhancement methods, face inherent limitations in multiphase systems, such as low mass transfer efficiency and uneven mixing [6–8]. Therefore, optimizing tank design and advancing stirrer innovation are crucial for enhancing mass transfer efficiency and improving gas–liquid contact in multiphase systems.

In recent years, design elements such as the optimization of stirring structures, improvement of gas distribution devices, and introduction of novel driving mechanisms have been widely explored to enhance the uniform distribution of bubbles, mass transfer performance, and flow-field characteristics within tanks [5,9,10]. Regarding stirring structure optimization, Gu *et al.* [11] designed a novel stirring paddle that effectively shortens the mixing time and enhances mass transfer. Regarding improvements to gas distribution equipment, Liu *et al.* [12] proposed a spherical microporous gas distributor whose microporous structure effectively reduced the bubble size. They increased the gas holdup and mass-transfer coefficient. Regarding novel drive mechanisms, Yip

* Corresponding author.
E-mail address: wanglinlin@gxu.edu.cn (L. Wang).

https://doi.org/10.1016/j.cjche.2026.03.018
1004-9541/© 2026 The Chemical Industry and Engineering Society of China, and Chemical Industry Press Co., Ltd. All rights are reserved, including those for text and data mining, AI training, and similar technologies.

et al. [5] proposed a vertical oscillation mechanism as an alternative to conventional mechanical stirring. They investigated the frequency dependence of gas–liquid mass transfer and fluid behavior in these tanks. These design elements have been shown to promote bubble dispersion, enhance mass transfer, and improve flow uniformity under the corresponding operational conditions [5,11,12]. However, these design elements suffer from restricted flow penetration and nonuniform bubble distribution. These drawbacks can be mitigated using liquid-driven equipment, which generates high shear and promotes more uniform bubble breakup.

Liquid jet-driven apparatuses, such as jet mixers and jet-loop tanks, have shown promise in enhancing mixing and mass transfer in multiphase systems [2,13]. Studies have shown that jet-driven apparatuses promote both internal liquid–gas recirculation and gas–liquid redispersion through intense jet penetration, thereby improving the overall performance within the tank [10,14]. These advantages arise from the elimination of traditional rotating shafts and impellers, the compact structure of the devices, and their adaptability to different tank sizes [2,15]. Although various developments have been reported for jet-driven apparatuses, a consensus on mitigating their structural and operational limitations remains elusive [15,16]. Many designs employ a single-nozzle configuration, which often restricts the spatial distribution of the liquid jets and consequently diminishes the mixing efficiency [10,17]. Furthermore, the number and orientation of the nozzles typically induce uneven flow patterns, and the gas phase often fails to disperse concurrently with the liquid phase, ultimately limiting gas–liquid mass transfer [10,18]. The simultaneous realization of efficient gas–liquid dispersion and effective mass transfer in jet-driven tanks remains an active area of research, as current approaches still show limitations in achieving multidirectional injection and generating multiscale bubbles [10,17,19]. Therefore, the structural optimization of tanks and innovative agitator designs represent practical approaches for mitigating the limitations of multiphase systems [20,21]. A novel agitator and gas injection method that simultaneously generates strong self-rotating flows and enhances bubble dispersion is an effective strategy for maximizing mass transfer efficiency in complex multiphase systems.

The bubble distribution, gas–liquid mass transfer, and flow field characteristics within the reactor are key factors governing the gas–liquid contact efficiency and mass transport behavior. The measurement, simulation, and quantitative characterization of the relevant features of the tank are required to elucidate the gas–liquid mixing mechanisms, optimize tank configurations, and advance agitator design. High-speed imaging coupled with digital image analysis provides a method for visualizing the geometric characteristics of bubbles [22,23]. The primary advantage of high-speed imaging techniques over probe-based measurement methods is their ability to capture accurate bubble information without the disturbances inherently introduced by physical probes, thereby ensuring more reliable and representative measurements [23,24]. The dynamic gassing-in method is a well-established and effective technique for determining the volumetric mass transfer coefficient (k_La), making it particularly suitable for assessing gas–liquid mass transfer efficiency [25,26]. The experimental characterization of flow field structures and turbulence characteristics within tanks has long been challenging because of optical inaccessibility and the intrusive nature of physical probes [27,28]. Notably, with the rapid advancement of computational fluid dynamics (CFD) techniques, the visualization of flow field structures and turbulent behaviors has become feasible, thereby enhancing the understanding of the coupled flow mechanisms within tanks [7,20,29,30].

Despite continuous progress in gas–liquid mixing and mass transfer intensification in tank systems, the understanding of liquid jet-driven apparatuses remains limited [15,16]. To the best of our knowledge, multi-nozzle, multi-layer hydraulically driven apparatuses capable of generating self-rotating flows and strong shear effects have rarely been reported. Methanol carbonylation is a typical gas–liquid multiphase reaction and an essential process for producing fundamental organic chemical feedstocks [31]. In this study, a novel multi-nozzle, multi-layer hydraulic agitator with semi-circular nozzles was proposed to address the limitations of conventional mechanically stirred and single-jet systems, enabling enhanced gas–liquid mixing and mass transfer within the tank. Unlike conventional impellers or injectors, the proposed configuration employs distributed radial jets and a layered structure to enhance axial circulation, tangential momentum transfer, and gas dispersion within a single device. The design utilizes asymmetric jet momentum to generate a self-rotating flow within the tank, thereby enhancing the liquid circulation and the intensity of gas–liquid mixing. Through experimental observations or numerical simulations, the bubble distribution, gas–liquid mass transfer, and flow field characteristics in a tank equipped with a hydraulic agitator were investigated under different operating conditions. The experimental results were compared with those obtained using mechanical stirring to highlight the benefits of hydraulic stirring on gas–liquid flow and mass transfer. Moreover, a pulsed intake mode was investigated to assess its potential impact on the gas–liquid mass transfer. CFD simulations provided further insights into the flow field characteristics within the tank, including the velocity field, turbulent kinetic energy (TKE), and turbulent dissipation rate (ε), which govern the bubble dispersion and mass transfer performance.

2. Experimental

2.1. Chemicals

Methanol (CH_3OH, analytical reagent) was obtained from Chengdu Cologne Chemical Co., Ltd. (Guangdong, China). Nitrogen and air (>99.99%) were obtained from Nanning Air Separation Gas Co., Ltd. (Nanning, China). Deionized water was prepared in the laboratory. Methanol, nitrogen, and air were selected as the working media, and all experiments were conducted under ambient conditions (25 ± 1) °C. The corresponding physical properties are listed in Table 1.

Although the study was conceptually motivated by methanol carbonylation, which relies on carbon monoxide, nitrogen was adopted as an inert surrogate owing to its comparable physicochemical properties and to circumvent the stringent safety and handling constraints associated with carbon monoxide.

2.2. Experimental apparatus

A schematic of the experimental apparatus is shown in Fig. 1(a). The setup consisted of a tank, a hydraulic agitator, a gas distributor, a temperature control unit, a data acquisition system, a piping control module, and a feedstock supply system. Table 2 lists the

Table 1
Physical properties of working media.

Working medium	Density/kg·m^{-3}	Dynamic viscosity/mPa·s	Surface tension/N·m^{-1}
Methanol	791.6	0.545	22.52
Nitrogen	1.165	0.018	
Air	1.184	0.0185	

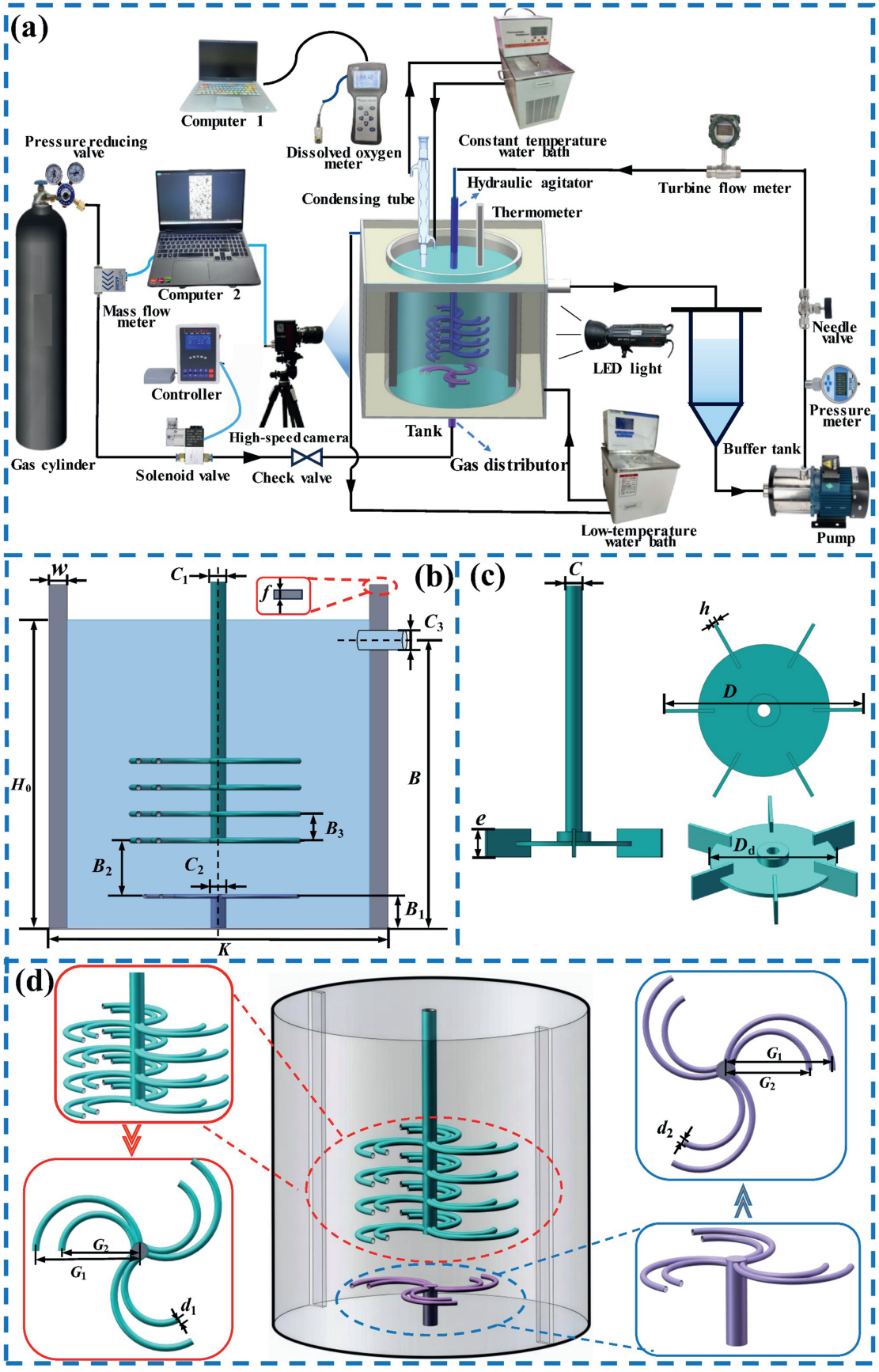


Fig. 1. Experimental system design: (a) schematic of the experimental setup; (b) schematic of the tank internal structure; (c) Rushton turbine configuration; (d) schematic of the hydraulic agitator and gas distributor.

Table 2
Experimental instrument specifications.

Instrument	Model	Manufacturer	Notes
Three-phase asynchronous motor	CHM2-6LSWSC	South Pump Industry Co., Ltd., China	Fated flow: 2 $m^3 \cdot h^{-1}$
High-speed camera	Phantom Miro R310	Vision Research, Inc., USA	Maximum frame rate: 3200 frames per second (full resolution); minimum exposure time: 1 μs (global shutter)
Gas flowmeter	AS200	Aosong Electronics Co., Ltd., China	Maximum range: 5 $L \cdot min^{-1}$
Solenoid valve	4V-210-08	AirTAC International Group (Airtac), Taiwan, China	Response time: <50 ms
Constant temperature water bath	LC-HCB-10	Shanghai Lichen Instruments Co., Ltd., China	Temp range: 5 °C–100 °C
Low-temperature water bath	DHC-2005-A	Hangzhou Qiwei Instruments Co., Ltd., China	Temp range: −20 °C to 100 °C
Dissolved oxygen meter	PDO-1000	Beijing Tengine Innovation Instruments Co., Ltd., China	Range: 0–20 $mg \cdot L^{-1}$
Flow velocity meter	LS1206B	Nanjing Xiangruide Electric Technology Co., Ltd., China	Flow range: 0.05–2.0 $m \cdot s^{-1}$

Table 3
Dimensions of the tank structural features.

Symbol	Value/mm	Symbol	Value/mm	Symbol	Value/mm
B	200	C_3	16	d_1	3
B_1	40	D	120	d_2	2
B_2	60	D_d	80	e	24
B_3	20	G_1	55	f	3
C	10	G_2	40	h	1.5
C_1	10	H_0	220	w	12
C_2	10	K	220		

primary instrumentation details. The central cylindrical flat-bottom tank was fabricated using transparent quartz glass. The internal structure is shown in Fig. 1(b), and the characteristic dimensions are listed in Table 3. Vertical baffles were mounted on the inner wall of the tank, and a rectangular insulated jacket was fitted on the outer surface and connected to the temperature control system. This jacket also minimizes optical distortion during visualization. In this study, three investigations were conducted. Although the same tank configuration was employed, the operating conditions were adjusted according to the specific objectives of each investigation. The feed flow rates were controlled using a turbine and mass flow meter, and data were collected using a high-speed camera, dissolved oxygen meter, and flow velocity meter.

2.3. The geometry of the hydraulic agitator and gas distributor

As shown in Fig. 1(d), this study developed a novel multi-nozzle, multi-layer self-rotating hydraulic agitator and a single-layer gas distributor. These were integrated into the tank to enhance liquid circulation and gas dispersion, with different layer configurations adopted to accommodate their distinct functional roles. Both were realized by incorporating multiple fine nozzles and optimizing their geometries and injection orientations. The characteristic dimensions are listed in Table 3. A qualitative comparison with representative existing impeller or injector is provided in Table 4 to illustrate the structural and operational features of the present design [10,17,18,32–34]. The hydraulic agitator consisted of a central pipe and four layers of semi-circular fine pipes. The multi-layer configuration allows liquid momentum to be introduced at multiple axial positions, thereby promoting vertically extended circulation within the tank. Each layer uniformly arranged six fine pipes of alternating large and small diameters, which were radially distributed along the horizontal plane with outward-oriented nozzles. The spacing between adjacent layers was fixed, and the entire assembly was positioned at equal intervals along the axial direction of the main feedpipe. The distributor was configured similarly to the hydraulic agitator and consisted of a single layer of fine tubes. This single-layer design was adopted to ensure effective gas introduction into the main circulation flow while avoiding flow interference associated with multi-layer gas injection. The working medium was injected through multiple nozzles to generate a strong tangential flow. This jet-induced momentum drove the bulk fluid into a self-rotating flow in the tank. Two types of horizontal installations were employed: co-directional (Co-dir) and counter-directional (Counter-dir), as shown in Fig. 2.

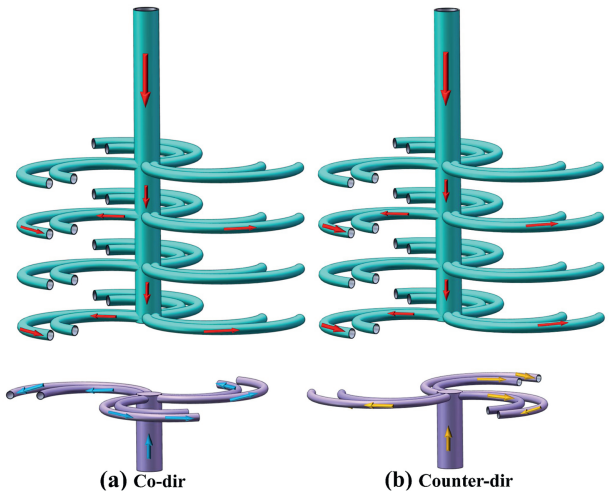


Fig. 2. Schematic of the hydraulic agitator and gas distributor orientations.

Table 4
Qualitative comparison of structural and operational features of the present agitator and representative existing impeller or injector.

Feature	Rushton turbine	Single-nozzle injector	Multi-nozzle injector	Hydraulic agitator (this work)
Driving mechanism	Mechanical rotation	Single jet-driven	Multi-point jet-driven	Jet-induced self-rotation and multi-point jet-driven
Momentum input way	Blade pumping	Single-jet	Multi-jets	Distributed multi-jets
Axial circulation	Moderate	Limited	Limited	Enhanced
Tangential momentum	Limited	Moderate	Moderate	Enhanced
Axial injection	Single level	Single level	Multi-level	Multi-level
Structural integration	Medium	Low	Medium	Integrated multi-layer

2.4. Experimental methodology

2.4.1. Bubbles and image processing

The image collection system comprised a high-speed camera, an LED lamp, and a computer, as shown in Fig. 1(a). The high-speed camera captured the bubbles in the circulating rising region through a transparent window, with the frame rate and resolution adjusted accordingly. The images were processed in batches using MATLAB and ImageJ in combination with digital image analysis to extract key bubble characteristics [23,35]. The overall image processing procedure is illustrated in Fig. S1 (in Supplementary Material). The images were first converted to grayscale and subjected to background subtraction to eliminate static interference and enhance the bubble foreground. Image enhancement was subsequently performed to improve boundary visibility, including Otsu-based adaptive thresholding (sensitivity = 0.4), median filtering (3×3 kernel), and Gaussian smoothing with a standard deviation of 2 pixels [36]. Bubble edges were accurately identified using the Canny edge detection operator with low and high thresholds of 0.1 and 0.3, respectively [37]. The detected contours were segmented through morphological opening and closing operations with a disk structuring element (radius = 1 pixel) to suppress noise and refine bubble boundaries. Subsequently, adjacent or partially overlapping bubbles were separated using a marker-controlled watershed algorithm, enabling the extraction of individual bubble contours, and their characteristic parameters were calculated [36,37].

The equivalent diameter (d_{eq}) of a bubble was calculated from its projected area (A) as follows [28,37,38].

$$d_{eq} = 2\sqrt{\frac{A}{\pi}} \tag{1}$$

The aspect ratio (E) is defined as the ratio of the minor axis (L_{minor}) to the major axis (L_{major}) of a bubble's minimum circumscribed circle (Eq. (2)) and is used to evaluate the degree of bubble deformation [39].

$$E = \frac{L_{major}}{L_{minor}} \tag{2}$$

The d_{32} was used to characterize the average bubble size [33,38,40], calculated as follows.

$$d_{32} = \frac{\sum n_i d_i^3}{\sum n_i d_i^2} \tag{3}$$

where d_i is the equivalent diameter of the i-th bubble, and n_i is the number of bubbles of that size.

The $\overline{E}$ quantifies the average shape change of bubbles [34], as in Eq. (4).

$$\overline{E} = \frac{\sum E_i}{n} \tag{4}$$

where E_i is the aspect ratio of the i-th bubble and n is the total number of bubbles.

2.4.2. Measurement of k_La

The k_La was measured using the classic dynamic gassing-in method [26,41]. During the experiment, after methanol was added to the tank, nitrogen was introduced to purge oxygen until the dissolved oxygen concentration dropped below 0.3 $mg \cdot L^{-1}$, at which point oxygen was considered removed. Subsequently, air was injected in pulsed or continuous modes through an externally controlled solenoid valve, while the dissolved oxygen concentration was monitored in real-time. Under pulsed conditions, the controller–solenoid valve system periodically opened and closed the valve to generate intermittent gas injection with preset pulse parameters. An oxygen sensor was positioned 170 mm from the bottom of the tank, and the signal was acquired using a dissolved oxygen meter. After temperature compensation and data smoothing, the measurements were linearly fitted to a first-order mass transfer model, with the slope representing k_La [25,42].

$$\mathrm{In}\left(\frac{C^* - C_0}{C^* - C_L}\right) = k_L a \tag{5}$$

where C^* denotes the saturated dissolved oxygen concentration, C_0 is the initial dissolved oxygen concentration in methanol, and C_L is the dissolved oxygen concentration at a specific time.

2.5. Numerical simulation

2.5.1. Governing equation

The finite volume method (FVM) was employed as the discretization framework to ensure the conservation of mass and momentum in liquid-phase flow [43]. The swirling flow in the tank was solely induced by the momentum of the high-velocity hydraulic jets. Therefore, rotating reference frames and sliding mesh techniques were not employed in the simulations. The realizable k–ε model was employed for turbulence closure, demonstrating superior accuracy in predicting shear-dominated and swirling flow dynamics, and was thus suited to the hydrodynamic conditions of this study. While advanced turbulence-induced bubble coalescence and breakup models have been developed for detailed multiphase CFD predictions [44,45]. The present study focuses on the characteristics of a single-phase flow field, and bubble characteristics were obtained experimentally rather than modeled numerically. The motion of incompressible fluids within tanks is governed by the continuity and Navier–Stokes equations, as follows [7,20,43,46].

Continuity equation:

$$\nabla \cdot \boldsymbol{u} = 0 \tag{6}$$

Navier–Stokes equation:

$$\frac{\partial(\rho \boldsymbol{u})}{\partial t} + \rho \boldsymbol{u} \cdot \nabla \boldsymbol{u} = -\nabla p + \mu \nabla^2 \boldsymbol{u} \tag{7}$$

where $\boldsymbol{u}$, ρ, μ, and p denote the velocity vector, fluid density, viscosity, and pressure, respectively.

The transport equations for TKE and ε are as follows [34,47].

$$\frac{\partial}{\partial t}(\rho k) + \frac{\partial}{\partial x_i}(\rho k u_i) = \frac{\partial}{\partial x_i}\left[\left(\mu + \frac{\mu_t}{\sigma_k}\right)\frac{\partial k}{\partial x_j}\right] + \tau_{ij}\frac{\partial u_i}{\partial x_j} - \rho\varepsilon \tag{8}$$

$$\frac{\partial}{\partial t}(\rho \varepsilon) + \frac{\partial}{\partial x_i}(\rho \varepsilon u_i) = \frac{\partial}{\partial x_i}\left[\left(\mu + \frac{\mu_t}{\sigma_\varepsilon}\right)\frac{\partial \varepsilon}{\partial x_j}\right] + C_{1\varepsilon}\frac{\varepsilon}{k}\tau_{ij}\frac{\partial u_j}{\partial u_j} - C_{2\varepsilon}\rho\frac{\varepsilon^2}{k} \tag{9}$$

where μ_t denotes the turbulence viscosity, $C_{1\varepsilon}$= 1.44, $C_{2\varepsilon}$= 1.92, σ_k= 1.0, and σ_ε= 1.3.

$$\mu = \frac{\rho C_\mu k^2}{\varepsilon} \tag{10}$$

where C_μ= 0.09.

2.5.2. Boundary conditions and solution setup

Considering the gravitational effects, the liquid inlet corresponding to the hydraulic jet was specified as a velocity inlet, and

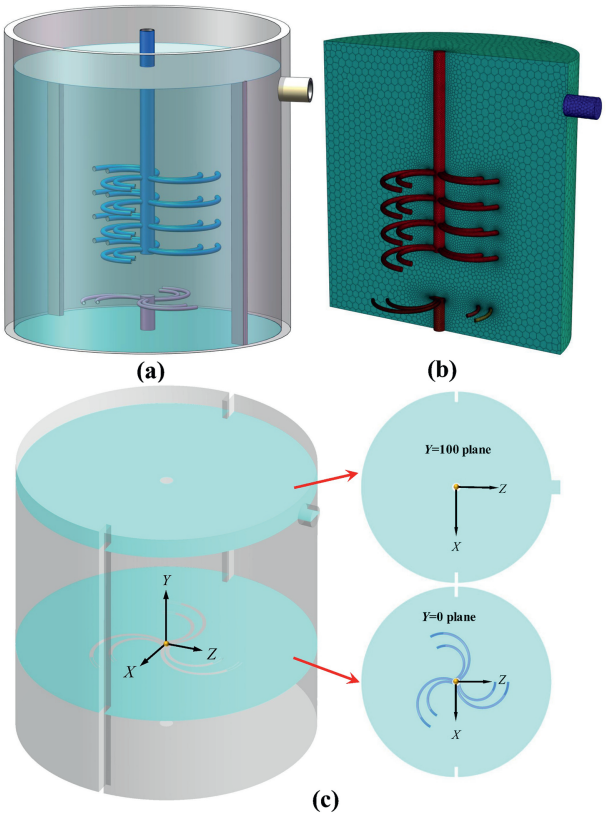


Fig. 3. Domain discretization and spatial representation: (a) geometry; (b) tank grid (grid numbers: 1.327 × 10^6); (c) coordinates.

the outlet was defined as a pressure outlet. The inlet velocity was determined based on the liquid circulation rates. All walls were treated as no-slip boundaries, and the wall pressure was set to zero. A pressure-based solver was employed, with pressure–velocity coupling implemented using the SIMPLE method [47]. The pressure and momentum equations were spatially discretized using second-order upwind schemes [11]. The simulations were performed transiently to capture the unsteady flow structures induced by the hydraulic-jet. A fixed time step of $\Delta t = 1 \times 10^{-3}$ s was adopted for all simulations, and no adaptive time stepping was applied. After an initial transient period, the flow field reached a statistically steady state. In addition to residuals, the volume-averaged velocity magnitude and TKE were monitored, and a statistical steady state was assumed when these variables showed negligible temporal fluctuations. The solution was considered converged when the residuals of all governing equations dropped below 1×10^{-4}, and the monitored global flow variables exhibited no further temporal drift.

2.5.3. Mesh independence test

Fig. 3(a) and (b) show the tank geometry from which the fluid domain was extracted for the CFD simulations. The domain was discretized using a hexahedral-dominant polyhedral mesh. Considering the size difference between the hydraulic agitator outlet and the tank diameter, local mesh refinement was applied in the jet region to resolve velocity gradients. The tank coordinate system is shown in Fig. 3(c).

A grid independence test was conducted using six different grid resolutions ranging from 5.361 × 10^5 to 1.889 × 10^6. Fig. 4 compares the time-averaged liquid-phase velocity magnitude and turbulent kinetic energy along the *X*-axis on the *XZ*-plane for the different grids. The relative difference between the medium and fine meshes was calculated as:

$$\delta = \frac{\left|\varphi_{\text{fine}} - \varphi_{\text{medium}}\right|}{\varphi_{\text{fine}}} \times 100\% \tag{11}$$

where φ represents key global flow quantities. The differences were below 2%, a commonly accepted threshold in CFD studies [48,49], indicating negligible discretization error and mesh-independent solutions. The flow distribution stabilized when the

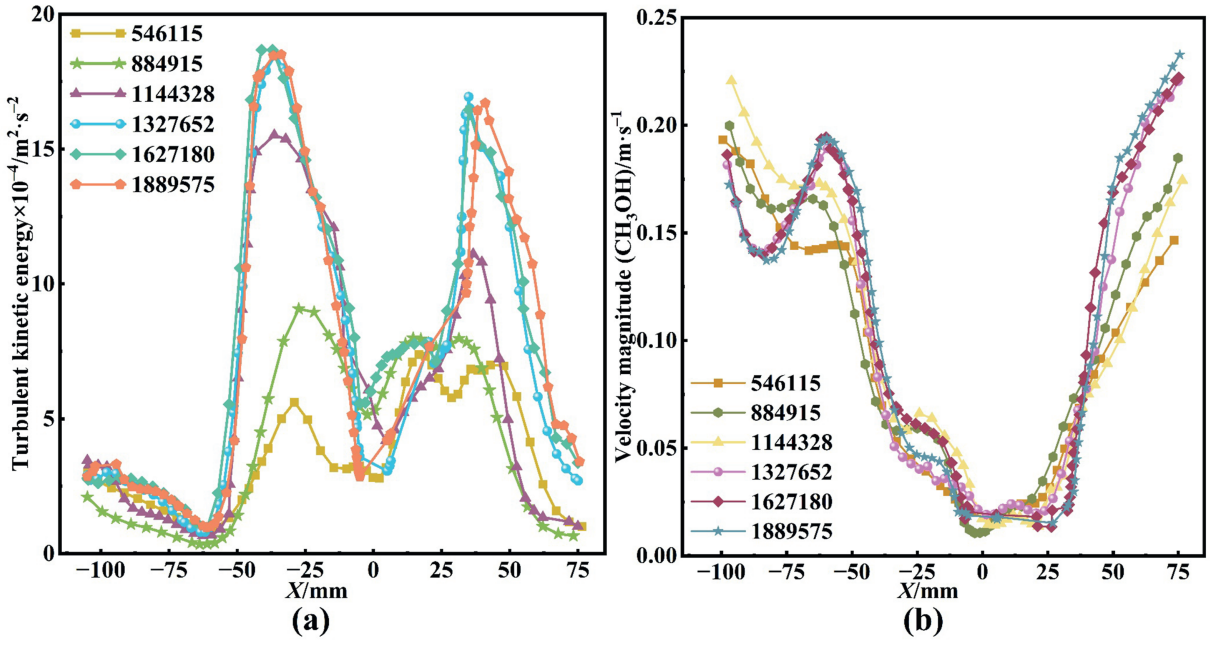


Fig. 4. Grid independence test: (a) mean turbulent kinetic energy distribution along the *X*-axis on the *XZ*-plane; (b) liquid-phase velocity distribution along the *X*-axis on the *XZ*-plane.

grid number reached approximately 1.327 × 10^6, and further refinement had a negligible effect on the simulation results. Therefore, a grid number of 1.327 × 10^6 was adopted for all subsequent transient simulations to achieve a balance between numerical accuracy and computational efficiency.

2.5.4. Validation of numerical results

To validate the numerical model, the simulated liquid-phase velocity was compared quantitatively with the experimental measurements. A vertical sampling line was defined on the *XZ*-plane at *X*= 50 mm, extending along the positive *Y*-axis at different heights. The velocity profiles along this line were extracted from the time-averaged results of the transient simulations to ensure consistency with the experimental measurements. As shown in Fig. 5, the simulated liquid-phase velocities at different vertical positions exhibited good agreement with the experimental measurement data, capturing both the magnitude and spatial variation trends. The results exhibited a strong correlation, demonstrating that the proposed model reliably predicts the liquid flow characteristics within the tank.

3. Results and Discussion

3.1. Bubble distribution characteristics

3.1.1. Bubble size distribution

Fig. 6 shows the effects of superficial gas velocity (u_g), liquid circulation rate (Q_v), baffle number (N), and gas distributor orientation on bubble size distribution. The results indicated that the bubble size distribution was sensitive to both the operational and structural parameters. As shown in Fig. 6(a), increasing the superficial gas velocity from 0.000219 to 0.001096 m·s^{-1} reduced the peak of the bubble size distribution by approximately 21% and increased the fraction of large bubbles. The distribution also shifted to the right, thereby broadening the size range [40]. As shown in Fig. 6(b), increasing the liquid circulation rate from 0.6 to 1.2 m^3·h^{-1} raised the peak of the distribution by approximately 28%, narrowed it toward smaller diameters, and increased the proportion of bubbles in the 0.5–2.0 mm range by 80%–85%, promoting a more uniform population. As shown in Fig. 6(c), the number of baffles had a non-monotonic effect on size distribution. When two baffles were employed, local vortices were effectively suppressed, and 75%–85% of the bubbles fell within the 0.5–2.0 mm range, making bubble refinement most effective. When the number of baffles exceeded two, the fraction of large bubbles increased, as excessive baffles caused short-circuiting and limited bubble break-up [50]. Notably, the counter-installed distributor produced a distribution that was 7%–18% narrower, with a peak height 6%–9% higher than that of the co-installed configuration, highlighting its effectiveness in refining bubbles and suppressing coalescence through enhanced local turbulence. Specifically, the combination of a lower superficial gas velocity, higher liquid circulation rate, two baffles, and a counter-installed distributor effectively controlled the bubble size distribution and optimized the gas–liquid dispersion performance.

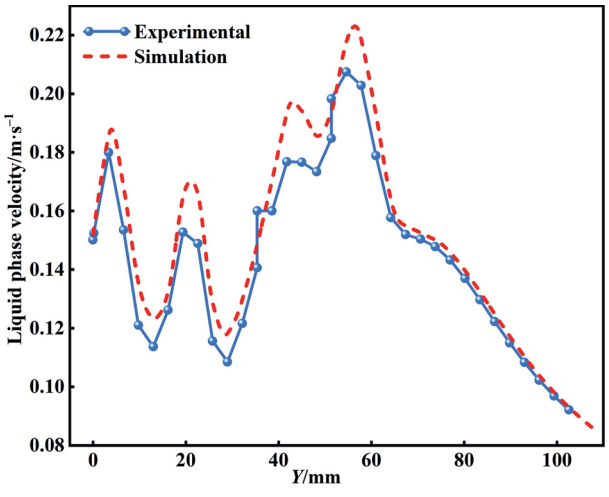


Fig. 5. Validation of the numerical model: liquid-phase velocity distribution along the positive *Y*-axis on the *XZ*-plane at *X*= 50mm.

3.1.2. Bubble shape distribution

Fig. 7 shows the effects of the superficial gas velocity, liquid circulation rate, baffle number, and distributor orientation on the bubble shape distribution. The results indicated that the interplay between operating conditions and structural parameters influenced the shape of the bubbles. As shown in Fig. 7(a) and (b), decreasing the superficial gas velocity or increasing the liquid circulation rate shifted the main peak of the shape distribution closer to 1. This change increased the fraction of near-spherical bubbles by 6%–14%, indicating a stronger tendency for sphericity. As shown in Fig. 7(c), the number of baffles affected the bubble shape. Two baffles produced the most concentrated distribution and optimal shape control, resulting in a 5%–14% higher fraction of high-aspect-ratio bubbles than the other configurations. Excessive baffles reduce the fraction of near-spherical bubbles, leading to shape instability [50]. The counter-installed distributor increased the occurrence of high-aspect-ratio bubbles (E> 0.8) by 6%–15% compared with the co-installed configuration, resulting in a bubble population with shapes closer to spheres [10]. This effect was attributed to the increased gas velocity, which enhanced the interfacial stretching and promoted longitudinal elongation. In contrast, liquid circulation and baffle-induced disturbances intensified the shear and regulated local turbulence to maintain shape consistency [9]. Specifically, the combination of a lower superficial gas velocity, higher liquid circulation rate, optimal baffle number, and counter-installed distributor promoted the formation of a near-spherical bubble population.

3.1.3. Sauter mean diameter

Fig. 8 shows the effects of the superficial gas velocity, liquid circulation rate, baffle number, and distributor orientation on the Sauter mean diameter of bubbles. The results indicated that both the operating parameters and structural configurations influenced the Sauter mean diameter. Increasing the superficial gas velocity enlarged the Sauter mean diameter by 10%–16% owing to enhanced bubble coalescence [51]. In contrast, increasing the liquid circulation rate reduced the bubble size by 35%–45% through stronger turbulent shear, promoting bubble refinement. The number of baffles has a non-monotonic effect on bubble size [9]. The two baffles achieved an optimal balance between turbulence intensity and flow disturbance, reducing the Sauter mean diameter by 2%–11%. Excessive baffles blocked the flow paths and enhanced the backflow, thereby limiting the bubble break-up. The counter-installed distributor enhanced bubble break-up and dispersion by altering the relative motion between the gas and liquid phases, resulting in a 4%–9% reduction in the Sauter mean diameter compared with the co-installed distributor.

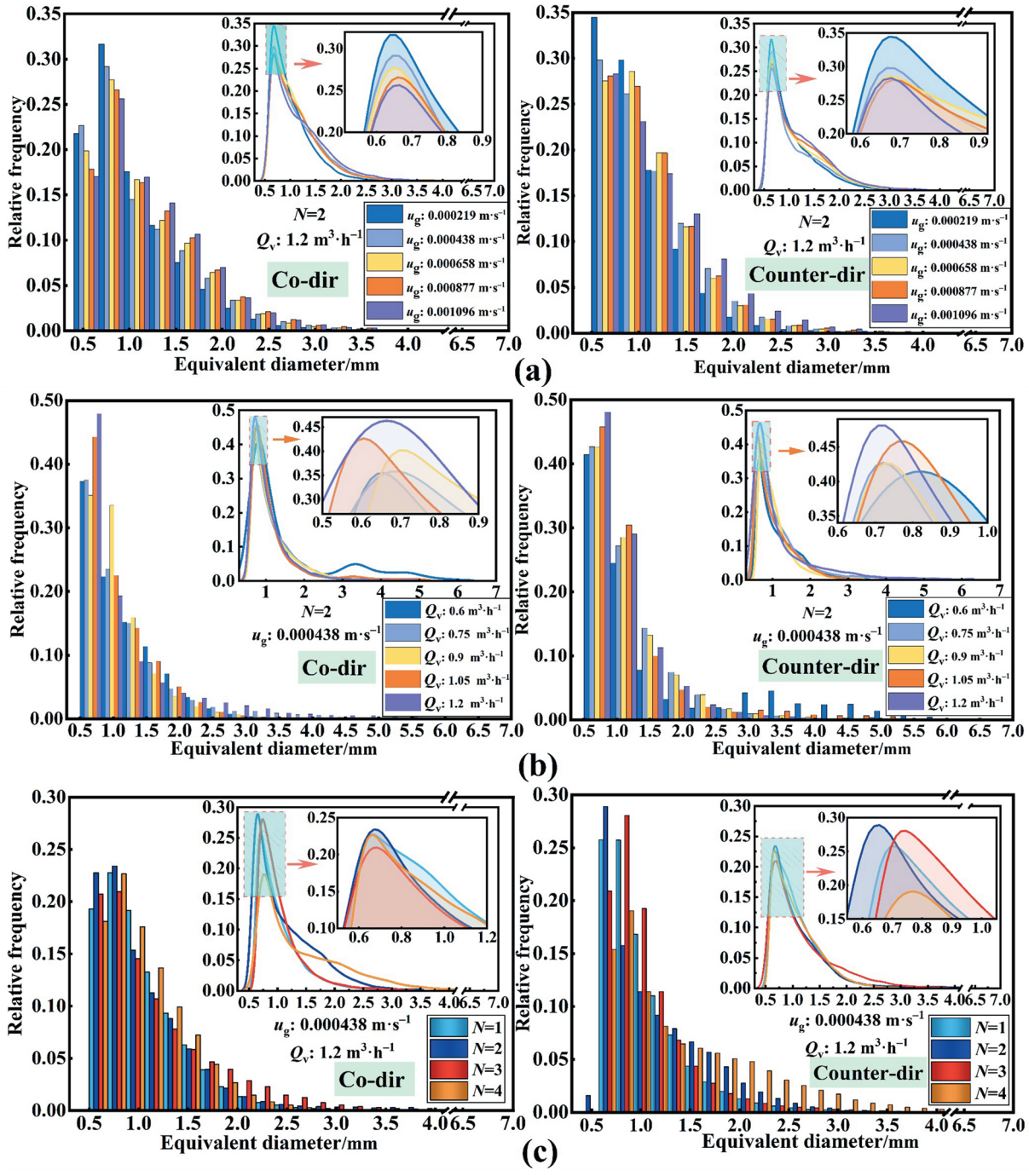


Fig. 6. Bubble size distribution under different conditions: (a) varying superficial gas velocity (Q_v= 1.2 $m^3 \cdot h^{-1}$, N= 2); (b) varying liquid circulation rate (u_g= 4.38 × 10^{-4} $m \cdot s^{-1}$, N= 2); (c) varying number of baffles (Q_v= 1.2 $m^3 \cdot h^{-1}$, u_g= 4.38 × 10^{-4} $m \cdot s^{-1}$).

3.1.4. Deformation rate

Fig. 9 illustrates the impact of superficial gas velocity, liquid circulation rate, baffle number, and distributor orientation on the bubble deformation rate. The results indicated that the combined effects of the operating parameters and structural configurations influenced the bubble deformation rate. As the superficial gas velocity increased, the deformation rate decreased by 6%–8.5%, indicating that the bubbles became more elongated [39]. In contrast, increasing the liquid circulation rate increased the deformation rate by 7%–13%, promoting bubble spheroidization. Increasing the number of baffles mitigated the variations induced by changes in the gas velocity and liquid circulation rate. With two or three baffles, the deformation rate increased by 6.5%–13%, reflecting enhanced bubble stability [9]. Distributor orientation also played a role: counter-installed, counter-directional gas–liquid jets enhanced turbulence and shear, whereas co-installed, co-directional jets formed a stable axial mainstream, reducing the deformation rate by 4%–5.5%. With four baffles, the difference between the distributor orientations was negligible, indicating that the multi-baffle arrangement dominated the local flow field.

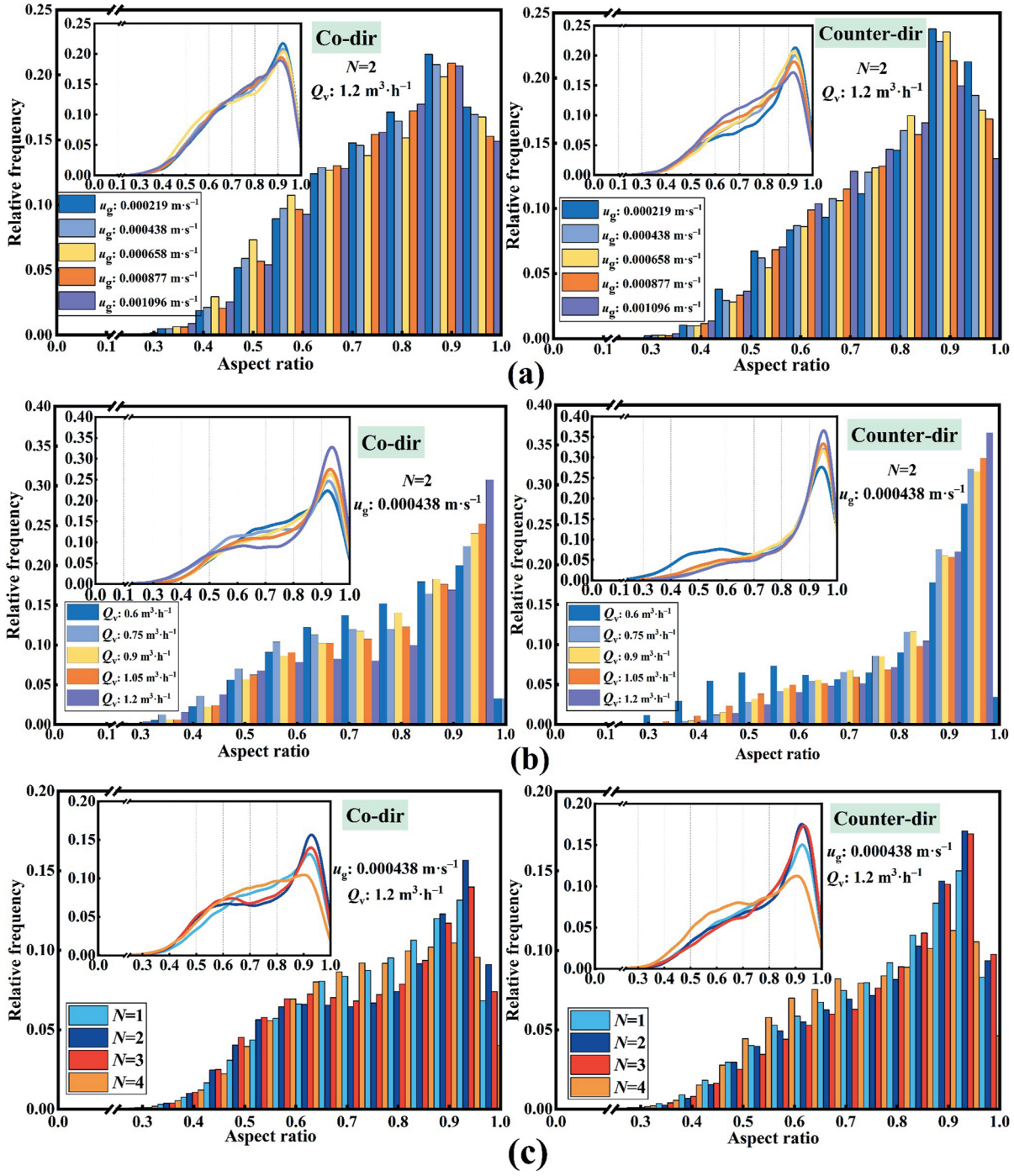


Fig. 7. Bubble shape distribution under different conditions: (a) varying superficial gas velocity (Q_v= 1.2 $m^3 \cdot h^{-1}$, N= 2); (b) varying liquid circulation rate (u_g= 4.38 × 10^{-4} $m \cdot s^{-1}$, N= 2); (c) varying number of baffles (Q_v= 1.2 $m^3 \cdot h^{-1}$, u_g= 4.38 × 10^{-4} $m \cdot s^{-1}$).

3.2. Mass transfer performance

The k_La is a key parameter for evaluating the gas–liquid mass transfer performance of a tank [41]. In this study, k_La was measured under two operating conditions: continuous and pulsed intake, with pulsing controlled by a solenoid valve.

3.2.1. Continuous intake

Under continuous intake mode, Fig. 10 shows the effects of superficial gas velocity, baffle number, and distributor orientation on k_La. As shown in Fig. 10(a), k_La increased by 145%–176% with increasing superficial gas velocity, reflecting the enhanced gas–liquid interface renewal process. Fig. 10(b) shows that the baffle structure exhibited nonlinear effects on the mass transfer. The k_La increased by 210%–290% as the number of baffles increased from zero to two, reaching a maximum, but decreased by 41%–49% when the number of baffles was further increased to four. Thus, moderate disturbance promotes bubble breakage and interface renewal, whereas excessive baffles reduce the mass transfer efficiency by hindering continuous bubble dispersion

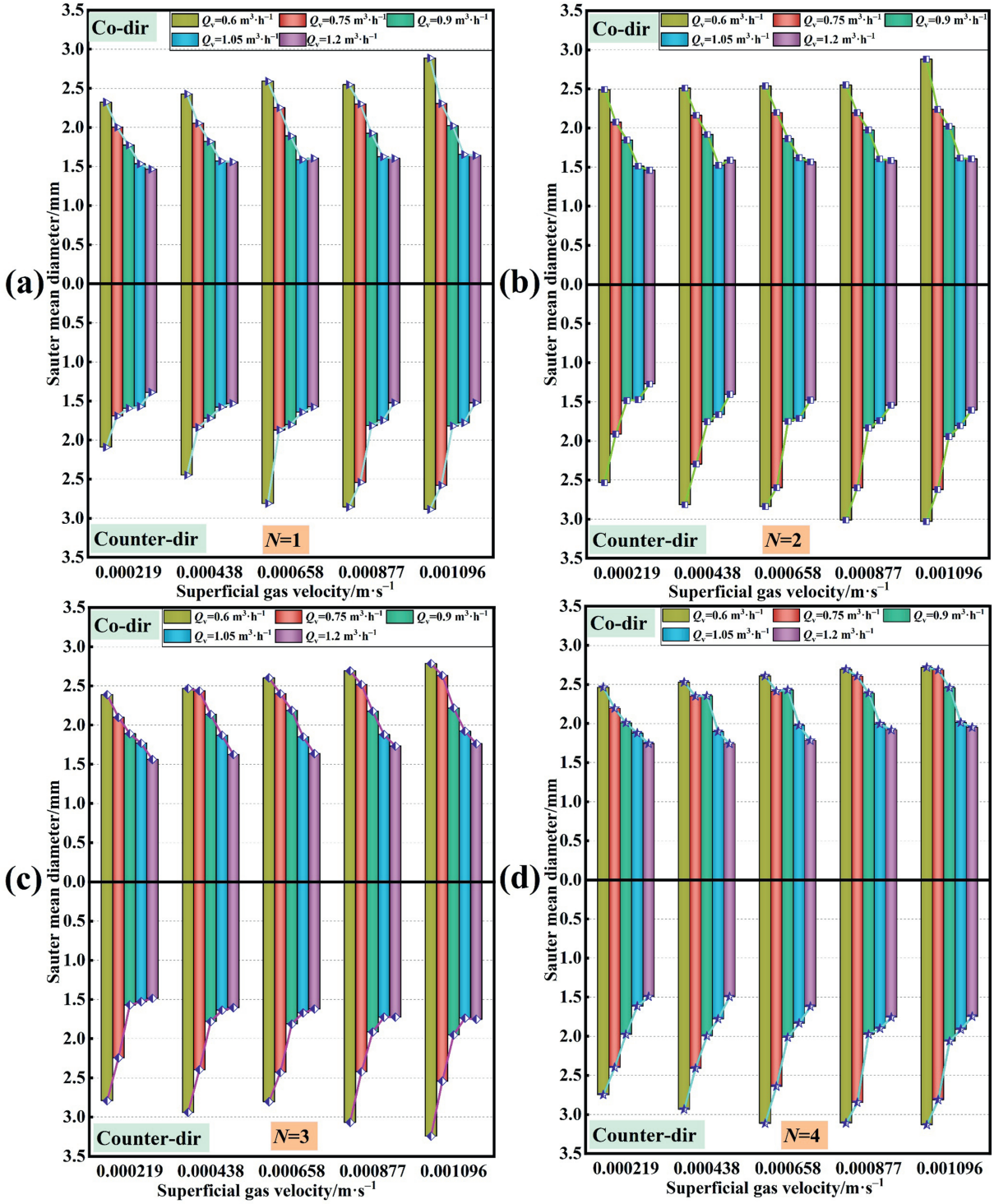


Fig. 8. Effects of superficial gas velocity, liquid circulation rate, and distributor orientation on bubble Sauter mean diameter for different numbers of baffles: (a) 1; (b) 2; (c) 3; (d) 4.

[9,33]. Distributor orientation also affected k_La: under identical conditions, the counter-installed distributor increased k_La by 6%–11% compared with the co-installed configuration, likely due to the induced radial recirculation that extended the bubble residence time and enlarged the effective mass transfer area. Although the difference between the orientations decreased at high gas velocities, the counter-installed distributor consistently exhibited superior mass transfer performance across the experimental range [10]. Specifically, the distributor orientation and baffle structure synergistically regulated mass transfer, with a high gas velocity, counter-installed distributor, and double-baffle structure effectively enhancing mass transfer. This conclusion aligns with Lacassagne *et al.* [52], who reported that "moderate turbulence structure helps to improve gas–liquid mass transfer efficiency".

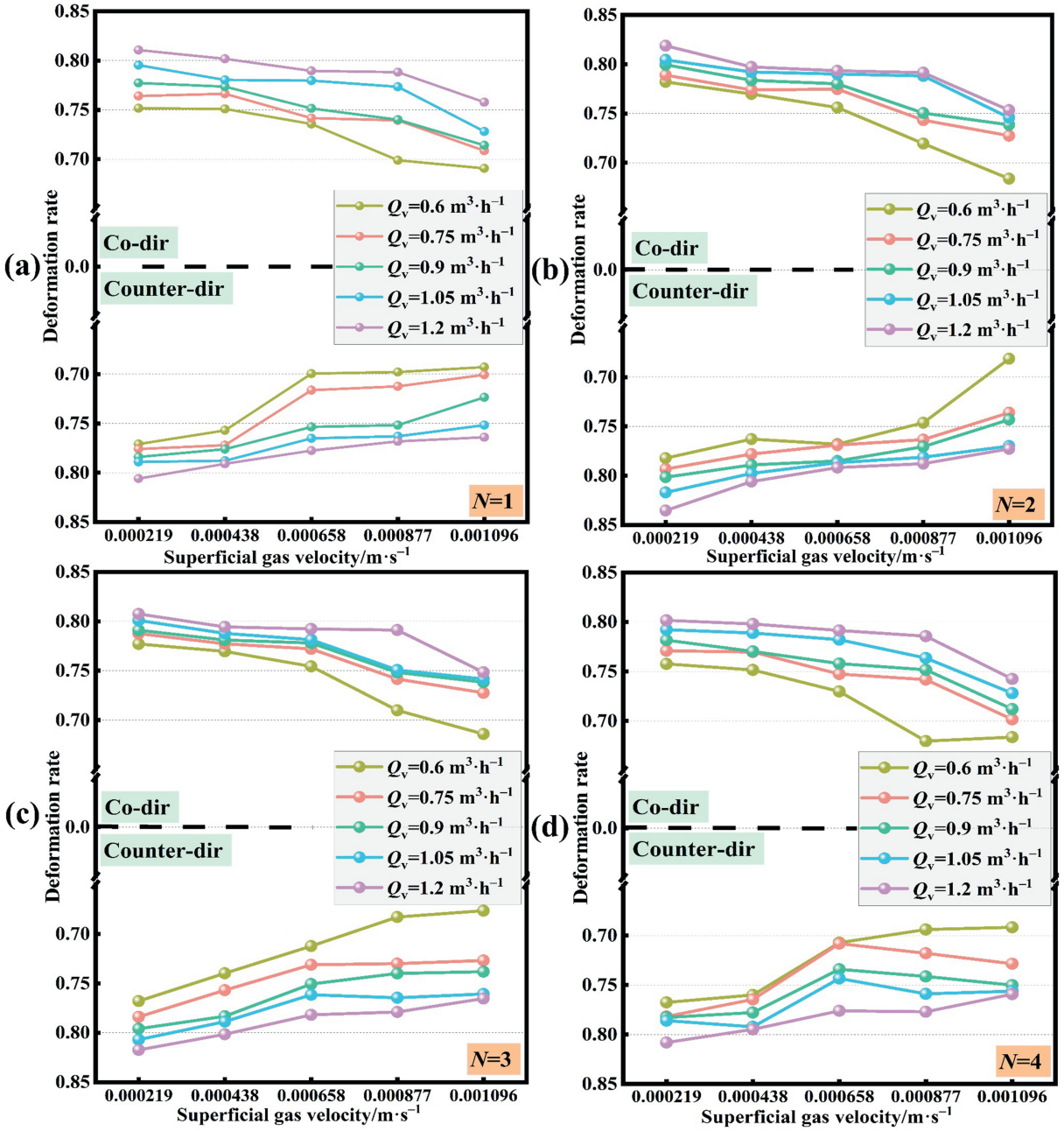


Fig. 9. Effects of superficial gas velocity, liquid circulation rate, and distributor orientation on bubble deformation rate for different numbers of baffles: (a) 1; (b) 2; (c) 3; (d) 4.

3.2.2. Pulse intake

Under pulse intake modes, Fig. 11 shows the effects of the pulse duty cycle (D_i), pulse period (T_i), and distributor orientation on k_La under various intake conditions.

As shown in Fig. 11(a) and (b), the intake mode and gas distributor configurations affected mass transfer, with k_La being 13%–20% higher under continuous intake than under pulsed intake [25]. The k_La increased by 83%–108% as the duty cycle increased from 0.1 to 0.5, but decreased by 51%–55% when the pulse period was extended from 0.5 s to 2.5 s, indicating that shorter pulse periods and higher duty cycles enhanced mass transfer efficiency. Mechanistically, the duty cycle governs the balance between gas injection and interruption, with higher duty cycles increasing the bubble renewal frequency and enhancing the liquid-phase disturbance [53]. Conversely, prolonged pulse periods reduce the bubble generation per unit time, thereby weakening gas–liquid mixing. This conclusion is consistent with that of Zhang *et al.* [54], who reported that moderate pulsation disturbances enhanced mass transfer. The effectiveness of pulsed intake depends on the match between the pulse frequency and the characteristic hydrodynamic time scales [34]. Based on Danckwerts' surface renewal theory, gas–liquid mass transfer is controlled by the interfacial renewal frequency [55,56]. When the pulse period exceeds the mixing or bubble renewal time, disturbances decay before the next injection, limiting interfacial renewal and mass transfer. Within the present operating range (0.5–2.5 s), the pulse period was comparable to or longer than the mixing time, explaining why the pulsed mode did not outperform continuous intake. Notably, k_La under high-duty-cycle pulsed operation gradually approached the values measured in the

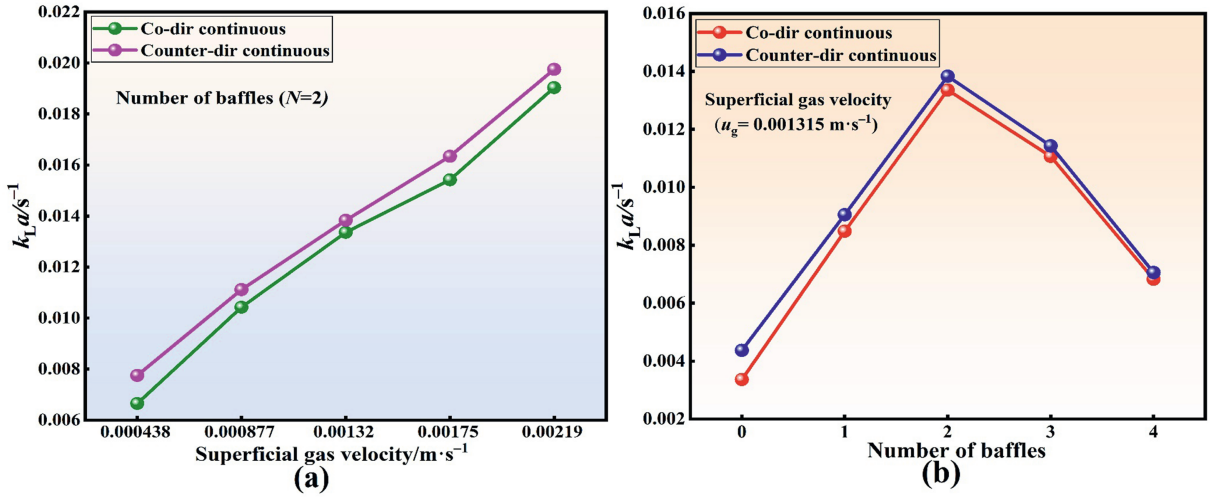


Fig. 10. Effects of baffle number, superficial gas velocity, and distributor orientation on k_La under continuous intake: (a) varying superficial gas velocity (N= 2); (b) varying number of baffles (u_g= 0.001315 m·s^{-1}).

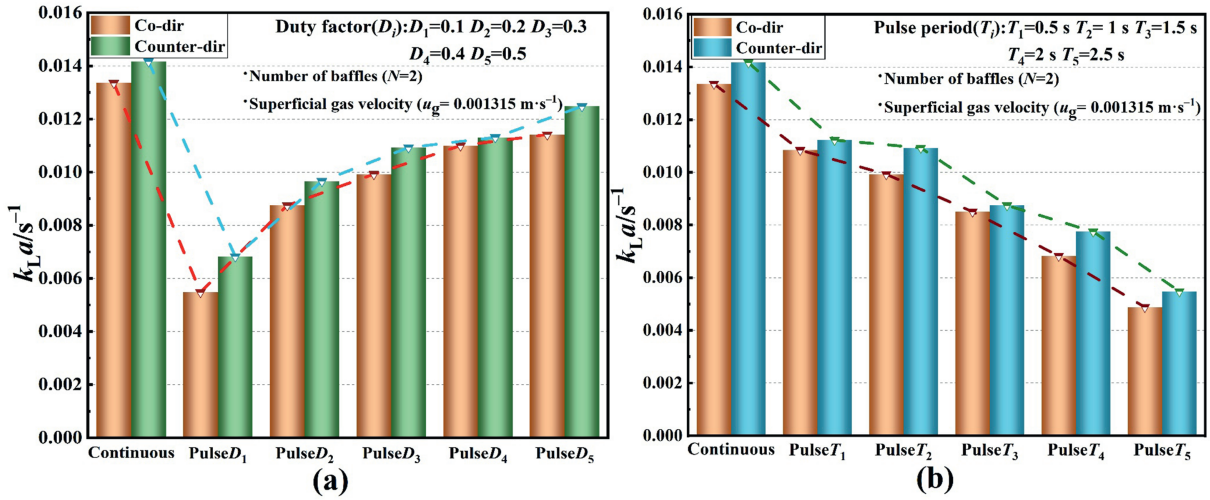


Fig. 11. Effects of intake mode and distributor orientation on k_La at N= 2 and u_g= 1.315 × 10^{-3} m·s^{-1}: (a) varying pulse duty cycle; (b) varying pulse period.

continuous intake mode. The counter-installed distributor consistently yielded a higher k_La, approximately 3%–10% higher than the co-installed configuration, thereby enhancing the effective mass transfer area through increased shear and promoting bubble break-up and redispersion. Specifically, the intake mode and distributor orientation synergistically regulated mass transfer, and the optimization of pulse parameters further improved the gas–liquid mass transfer efficiency, although it remained lower than that under continuous intake.

3.3. Comparison of mechanical stirring and hydraulic stirring

This study employed the power ratio method to comparatively analyze mechanical and hydraulic stirring under equivalent energy input conditions by normalizing the power [41,57]. By adjusting the operating parameters, both stirring modes were operated under identical power per unit volume conditions, eliminating the influence of power differences on the results. Mechanical stirring was conducted using a six-blade Rushton turbine with the configuration shown in Fig. 1(c) and the characteristic dimensions listed in Table 3. This Rushton turbine was selected as a representative radial-flow type widely used as a benchmark in gas–liquid mixing studies because of its well-documented hydrodynamic and mass transfer characteristics [32,58–60]. The Supplementary Material details the parameter selection and calculation steps for both stirring modes while maintaining constant power per unit volume.

A pump powered the hydraulic stirring tank. The power per unit volume was calculated using the following equation [61].

$$P_j = \rho g Q_v H_j \tag{12}$$

$$P_{v,j} = \frac{P_j}{V_j} \tag{13}$$

where P_j is the hydraulic stirring power, g is the gravitational acceleration, Q_v is the liquid circulation rate during hydraulic stirring, H_j is the pump head under hydraulic stirring conditions, and V_j is the working volume of the hydraulic stirring tank.

The power of the mechanical stirring tank is the sum of the stirrer shaft and circulation pump powers. The power per unit volume was calculated using the following equations [61,62]:

$$P_m = N_p \rho N_r^{\ 3} D^{\ 5} + \rho g Q_m H_m \quad (14)$$

$$P_{v,m} = \frac{P_m}{V_m} \quad (15)$$

where P_m is the mechanical stirring power, N_p is the power number of the Rushton turbine, N_r is the stirring rotational speed, D is the Rushton turbine diameter, Q_m is the liquid circulation rate during mechanical stirring, H_m is the pump head under mechanical stirring conditions, and V_m is the working volume of the mechanical stirring tank.

For a typical Rushton turbine operating unventilated in a fully turbulent regime, the reported N_p values generally range from 4.5 to 6.5, with an empirical value of approximately five commonly used [32,61]. Under gas–liquid two-phase conditions, the presence of bubbles reduces the effective power number by decreasing the stirring efficiency compared with the single-phase case. Studies have shown that the power of a Rushton turbine can decrease by approximately 10%–30% under ventilated conditions, depending on the gas flow rate and operating Reynolds number [33,63]. Accordingly, this study adopted the air-free power value (N_p= 5) from the literature and applied a gas content correction factor using the power number correlation curve proposed by Kaiser *et al.* [57] to accurately represent the actual energy consumption under gas–liquid conditions.

This section ensures that experiments were conducted under conditions in which both systems operated at identical power per unit volume.

$$P_{v,m} = P_{v,j} \quad (16)$$

3.3.1. Comparison of bubble distribution characteristics

3.3.1.1. Bubble size distribution. Fig. 12 illustrates the impact of superficial gas velocity on the bubble size distribution under four operating conditions with two baffles and a power per unit volume of 7550 W·m^{-3}. The results indicated that the bubble size distribution shifted toward larger diameters as the superficial gas velocity increased [33]. As shown in Fig. 12(a), under hydraulic stirring, the modal bubble diameter primarily ranged from 0.5 to 2 mm, accounting for over 75% of the population and resulting in a

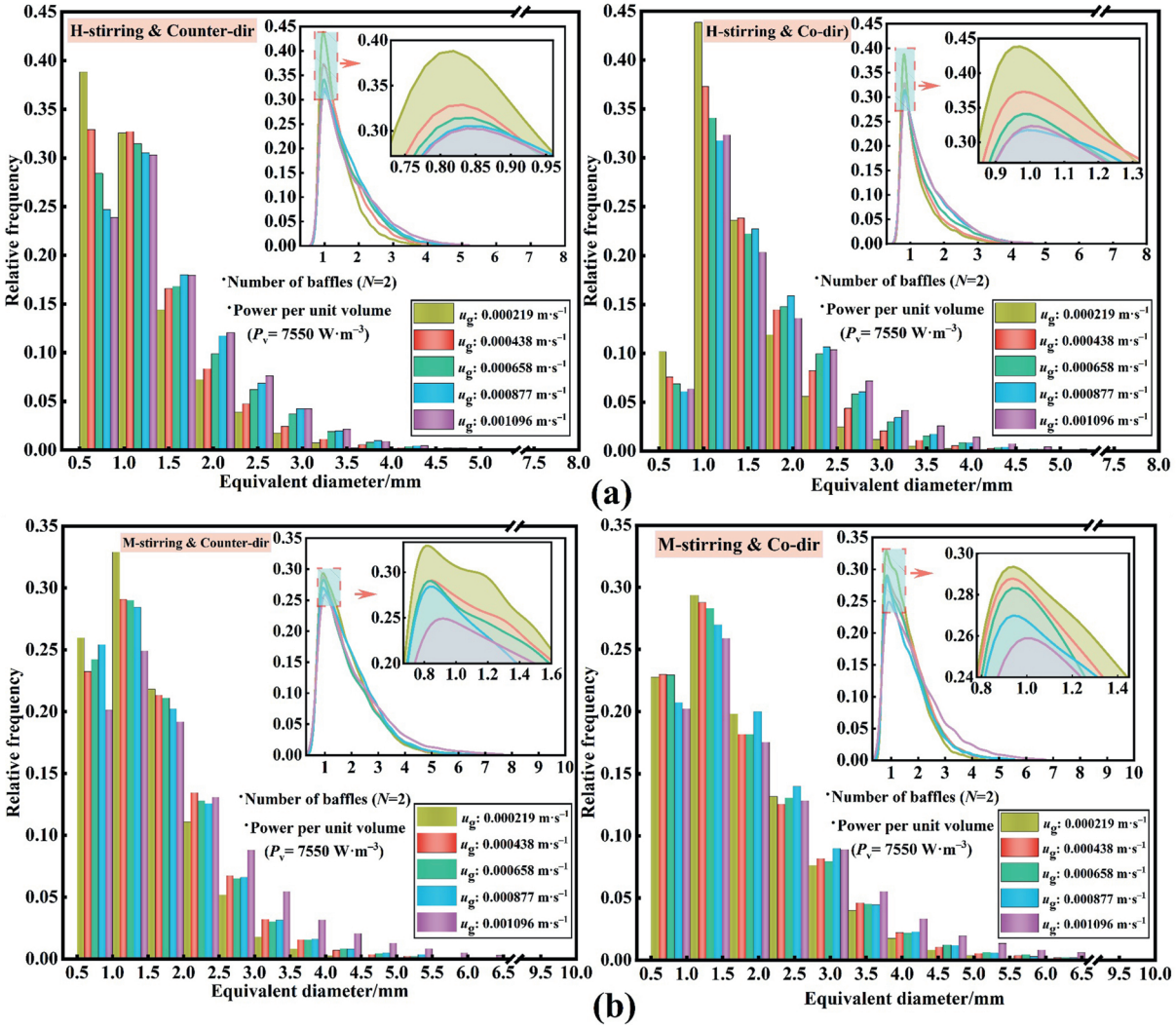


Fig. 12. Effects of stirring mode, distributor orientation, and u_g on bubble size distribution at N= 2 and P_v= 7550 W·m^{-3}: (a) hydraulic stirring; (b) mechanical stirring.

compact distribution that reflected a high degree of bubble refinement. In contrast, Fig. 12(b) shows that mechanical stirring yielded a broader distribution with an extended tail and approximately twice the proportion of bubbles larger than 2 mm, indicating weaker bubble break-up. This difference arose from distinct bubble formation mechanisms: hydraulic stirring depended on jet-induced vortices and shear, facilitating continuous breakage and circulation, whereas mechanical stirring produced strong local shear and low-velocity regions that promoted coalescence [41]. Further comparison revealed that, under identical gas velocities and distributor configurations, hydraulic stirring consistently generated smaller and more narrowly distributed bubbles, exhibiting superior size control and distribution stability. Notably, the counter-installed distributor reduced the bubble diameter by 5%–8% in both modes, with the reduction under hydraulic stirring being nearly 1.5 times that under mechanical stirring, indicating a synergistic effect on bubble break-up.

3.3.1.2. Bubble shape distribution. Fig. 13 illustrates the impact of superficial gas velocity on bubble shape distribution under four operating conditions with two baffles and a power per unit volume of 7550 W·m^{-3}. The results indicated that the bubble aspect ratio predominantly ranged from 0.6 to 0.95 across all conditions, suggesting that most bubbles adopted near-spherical shapes [33,39]. As shown in Fig. 13(a), under hydraulic stirring, approximately 55%–60% of bubbles exhibited a high aspect ratio (E > 0.75), with the distribution shifted toward higher values and becoming more concentrated, particularly in the presence of the counter-installed distributor. In contrast, Fig. 13(b) shows that mechanical stirring yielded a broader distribution, with only 35%–50% of the bubbles having an E value greater than 0.75, indicating greater deformation. This difference arose from the underlying mechanisms: hydraulic stirring relied on jet-induced stable shear and circulation to enhance bubble sphericity under relatively uniform stretching, whereas localized intense shear and non-uniform turbulence during mechanical stirring generated uneven stress on bubbles, readily producing irregular shapes such as ellipsoids [39]. Overall, hydraulic stirring maintained a high consistency in bubble morphology across different operating conditions, highlighting its stability and superiority for microbubble control.

3.3.1.3. Sauter mean diameter and deformation rate. Fig. 14 illustrates the impact of superficial gas velocity on the Sauter mean diameter and deformation rate of bubbles under four operating conditions with two baffles and a power per unit volume of

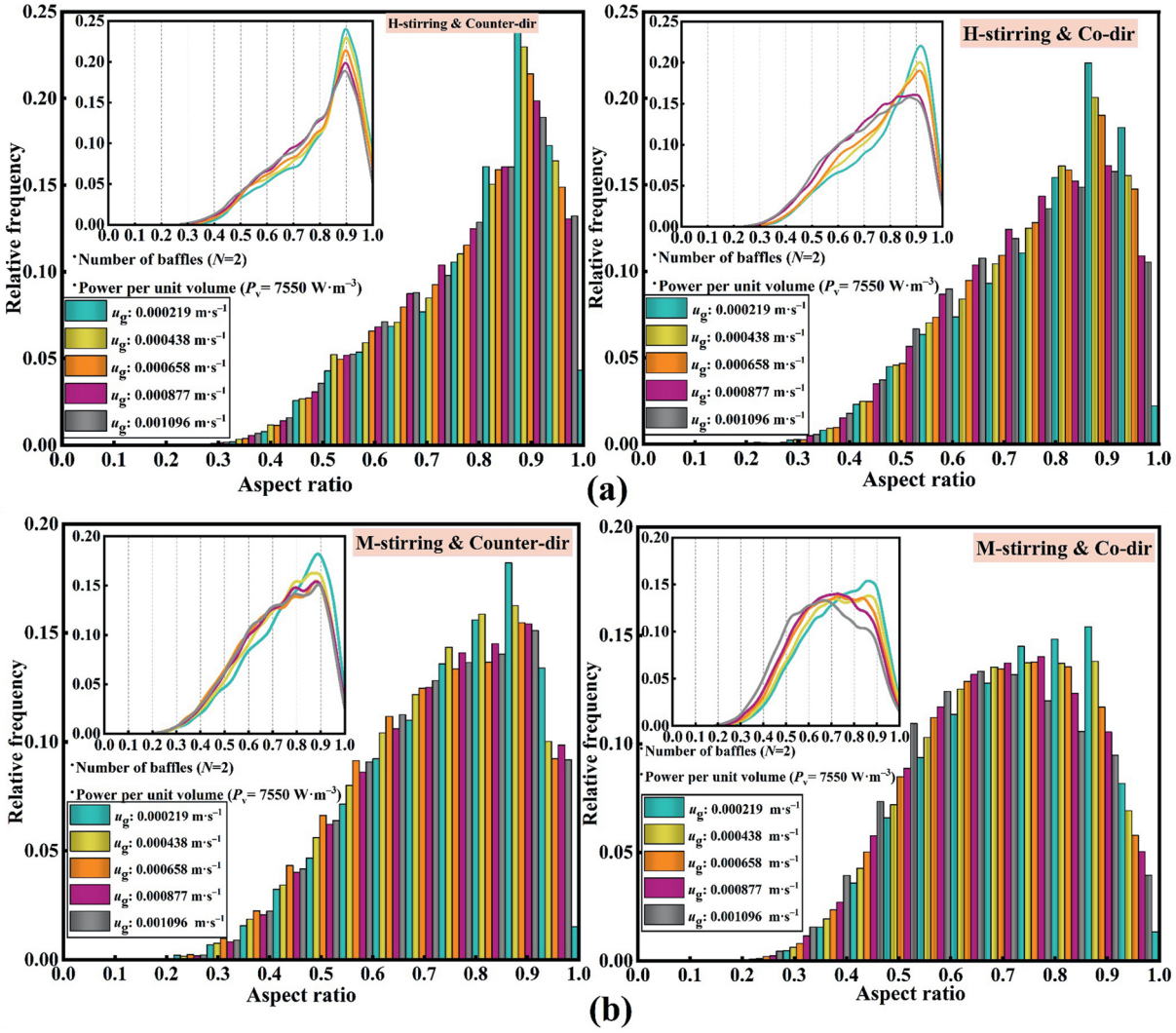


Fig. 13. Effects of stirring mode, distributor orientation, and u_g on bubble shape distribution at N= 2 and P_V= 7550 W·m^{-3}: (a) hydraulic stirring; (b) mechanical stirring.

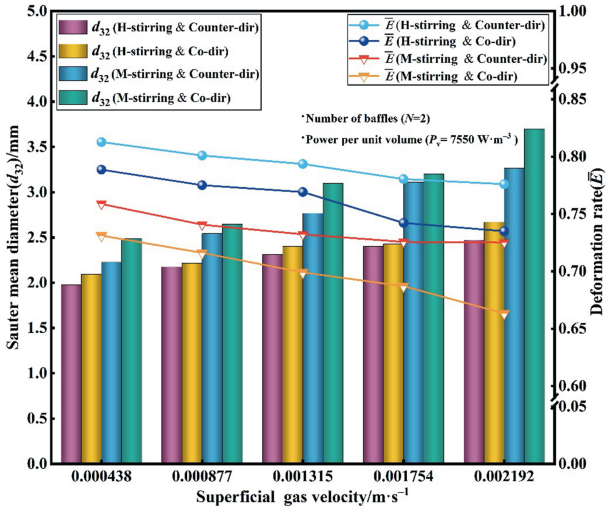


Fig. 14. Effects of stirring mode, distributor orientation, and superficial gas velocity on bubble Sauter mean diameter and deformation rate at N= 2 and P_V= 7550 W·m^{-3}.

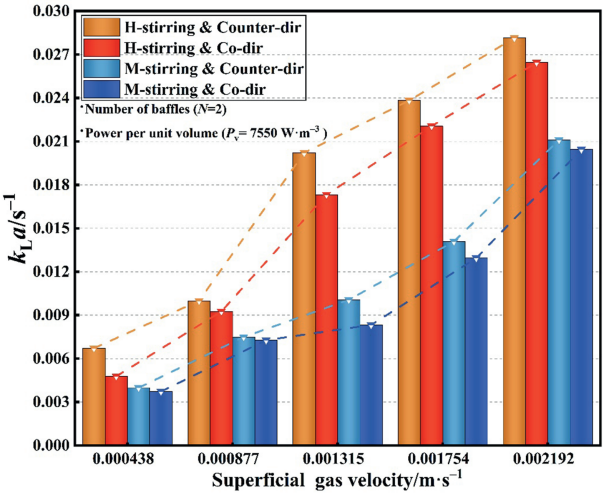


Fig. 15. Effects of stirring mode, distributor orientation, and superficial gas velocity on k_La at N= 2 and P_V= 7550 W·m^{-3}.

7550 W·m^{-3}. The results indicated that, within the investigated range of superficial gas velocities, the Sauter mean diameter under mechanical stirring was consistently 25%–40% larger than under hydraulic stirring, reaching a maximum of 3.7 mm with the co-installed distributor [64]. Hydraulic stirring produced smaller bubbles, averaging 1.9–2.3 mm, with a more uniform and narrowly dispersed distribution. The deformation rate analysis revealed that hydraulic stirring maintained a higher average deformation rate of 0.78, preserving near-spherical bubble shapes. In contrast, mechanical stirring resulted in a lower rate of 0.71, with deviations from sphericity increasing as gas velocity increased [39]. From a fluid dynamics perspective, hydraulic stirring generates stable circulating flow fields using high-speed jets, effectively suppressing bubble coalescence. In contrast, mechanical stirring induces uneven breakup and re-coalescence owing to localized high shear, resulting in greater fluctuations in the bubble shape. Notably, under both stirring modes, the counter-installed distributor reduced the Sauter mean diameter by 4%–8% and increased the deformation rate by 4%–5%, likely due to the bubble rectification effect induced by the interaction of the gas and liquid jet directions. Overall, hydraulic stirring demonstrated advantages in controlling the bubble size and maintaining the bubble shape.

3.3.2. Comparison of mass transfer performance

Fig. 15 illustrates the impact of superficial gas velocity on k_La under four operating conditions, with two baffles and a power per unit volume of 7550 W·m^{-3}. The results showed that k_La increased with increasing superficial gas velocity under all operating conditions. The maximum k_La achieved under hydraulic stirring combined with the counter-installed distributor was approximately 1.4–1.8 times higher than that achieved under mechanical stirring with the co-installed distributor. Within the examined gas velocity range, k_La increased by 6%–16% depending on the configuration, and hydraulic stirring enhanced k_La by 20%–45% compared with that of mechanical stirring. The mass transfer coefficient is affected by the renewal frequency of the gas–liquid interface and local shear strength [52,65]. Hydraulic stirring prolongs the bubble residence time and enhances interfacial turbulence *via* circulation-driven flow. Coupled with the countercurrent gas–liquid motion induced by the counter-installed distributor, it enlarges the gas–liquid contact area and thereby improves the mass transfer efficiency. In contrast, mechanical stirring generates localized high shear primarily around the impeller blades, leading to limited bubble break-up near the wall and a reduced overall mass transfer performance. Notably, the counter-installed distributor improved the mass transfer performance of the tank, resulting in a 7%–11% increase in k_La compared with the co-installed configuration. Specifically, hydraulic stirring enhances gas–liquid interface renewal and mass transfer, whereas optimizing the distributor configuration remains equally crucial.

3.4. Flow field simulation results

CFD simulations were performed to characterize the flow field in the hydraulic stirring tank. The analysis focused on three representative quantities: the velocity field, TKE, and ε, which collectively describe the momentum transport, turbulence generation, and energy dissipation that govern tank performance [29,66]. The analysis of these parameters elucidated how the jet-induced flow structures influenced fluid circulation, mixing intensity, and local energy distribution.

3.4.1. Velocity field analysis

Fig. 16 shows the velocity distribution in the tank jet zone (Y= 0 plane) under different conditions. The results indicated velocity

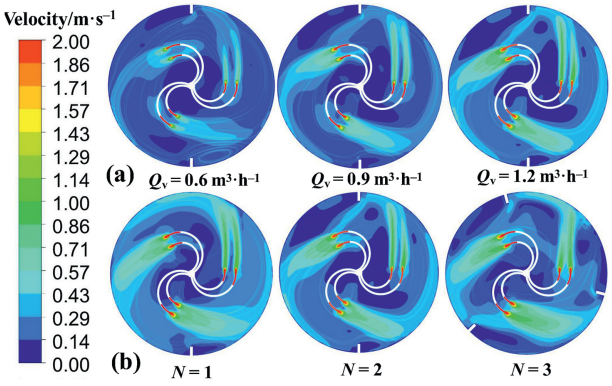


Fig. 16. Velocity distribution in the tank jet zone under various conditions (Y= 0 plane): (a) varying liquid circulation rate (N= 2); (b) varying number of baffles (Q_V= 1.2 m^3·h^{-1}).

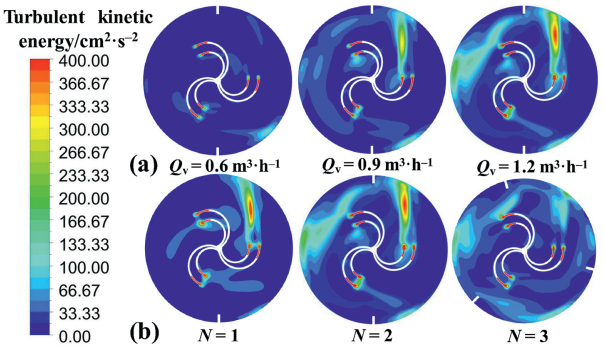


Fig. 17. The TKE distribution in the tank jet zone under various conditions (Y= 0 plane): (a) varying liquid circulation rate (N= 2); (b) varying number of baffles (Q_v= 1.2 $m^3 \cdot h^{-1}$).

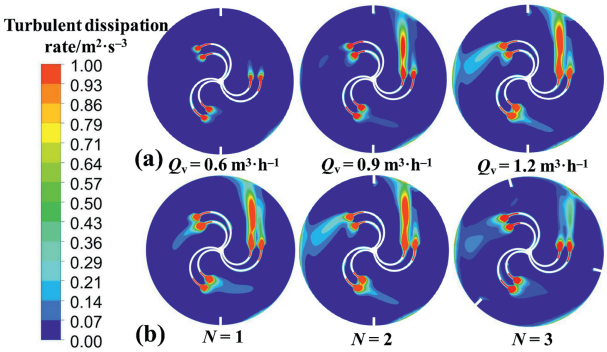


Fig. 18. The ε distribution in the tank jet zone under various conditions (Y= 0 plane): (a) varying liquid circulation rate (N= 2); (b) varying number of baffles (Q_v= 1.2 $m^3 \cdot h^{-1}$).

peaks at the six fine-tube nozzles and their wakes, which served as the primary driving forces for liquid circulation. Simultaneously, low-velocity recirculation zones were observed near the walls. As shown in Fig. 16(a), an increase in the liquid circulation rate increased the flow velocity, expanded the circulation pathways, and enhanced the transport capacity of the main circulation. The high-velocity zone extended both radially and circumferentially, while the low-velocity recirculation zone contracted yet persisted under these conditions [17]. As shown in Fig. 16(b), increasing the number of baffles disrupted large-scale vortices, resulting in a more heterogeneous momentum distribution, the formation of multiple local recirculation cells, and additional small-scale stagnation zones in the baffle-shadowed regions [9].

3.4.2. Turbulent kinetic energy analysis

Fig. 17 shows the TKE distribution in the tank jet zone (Y= 0 plane) under various conditions. The results indicated that the six fine-tube nozzles and their wake regions generated regions with high TKE. In contrast, low-TKE regions were observed in the surrounding areas and downstream of the baffles [17]. As shown in Fig. 17(a), increasing the liquid circulation rate enhanced the overall TKE and expanded the turbulent thickness within the circulation channel, indicating improved energy transfer resulting from higher liquid flow rates [67]. The TKE distribution exhibited both radial and circumferential extensions, with localized low-energy regions persisting despite the intensified turbulent shear forces induced by the elevated velocities. As shown in Fig. 17(b), increasing the number of baffles disrupted large-scale vortices, forming multiple localized high-TKE zones downstream of the baffles. This increase promoted local mixing, although an excessive number of baffles created shielded low TKE zones.

3.4.3. Turbulent dissipation rate analysis

Fig. 18 shows the distribution of ε in the tank jet zone (Y= 0 plane) under various conditions. The results indicated that the six fine-tube nozzle outlets and their wake regions generated high-dissipation zones, which reflected strong velocity gradients and localized turbulent dissipation [34]. In contrast, the near-wall regions, areas downstream of the baffles, and vortex wakes generated low-dissipation zones, which corresponded to far-field areas of energy transfer. As shown in Fig. 18(a), increasing the liquid circulation rate elevated the overall ε. It expanded the high-dissipation zone, indicating that higher liquid-phase flow rates intensified shear effects and increased energy levels [34]. The dissipation distribution extended along the primary flow direction, with ε peaking in the high-shear regions, consistent with the enhanced energy transfer to smaller scales. As shown in Fig. 18(b), increasing the number of baffles fragmented the large-scale energy into localized shear layers, generating dispersed high-dissipation zones that promoted local mixing. Simultaneously, low-dissipation stagnation zones formed in regions shielded by the baffles [28].

3.5. Analysis of gas–liquid interaction mechanisms

In multiphase mixing systems, the interaction between bubbles, turbulence, and vortices critically shapes the observed macroscopic hydrodynamics and mass transfer behavior [33,68]. Based on the experimental observations and CFD results presented earlier, we analyzed the internal mechanisms that give rise to the characteristic bubble distribution, gas–liquid mass transfer patterns, and flow field structures under different operating conditions. The corresponding mechanistic interpretation is summarized in Fig. 19 and discussed below.

(1) As shown in Fig. 19(a), the mixing was dominated by self-rotating vortices. The jet-induced swirling motion generates large vortical structures that interact with smaller-scale eddies, promoting bubble dispersion and enhancing interfacial renewal.
(2) As shown in Fig. 19(b), the high-velocity shear effect intensified local energy dissipation. The turbulence generated at the hydraulic agitator outlet promotes bubble breakup, producing smaller and more widely dispersed bubbles, thereby improving spatial uniformity.
(3) Fig. 19(c) highlights the role of multi-zone flow coupling in the mixing process. Radial injection through fine tubes establishes an annular self-rotating flow that drives the formation of a dominant axial stream. The coupling between these regions enhances the macroscopic gas–liquid transport.
(4) As illustrated in Fig. 19(d), gas entrainment into the liquid stream intensifies gas–liquid interactions, generating liquid-driven forces that break bubbles into finer sizes and prolong their residence time, thereby enhancing gas–liquid contact.

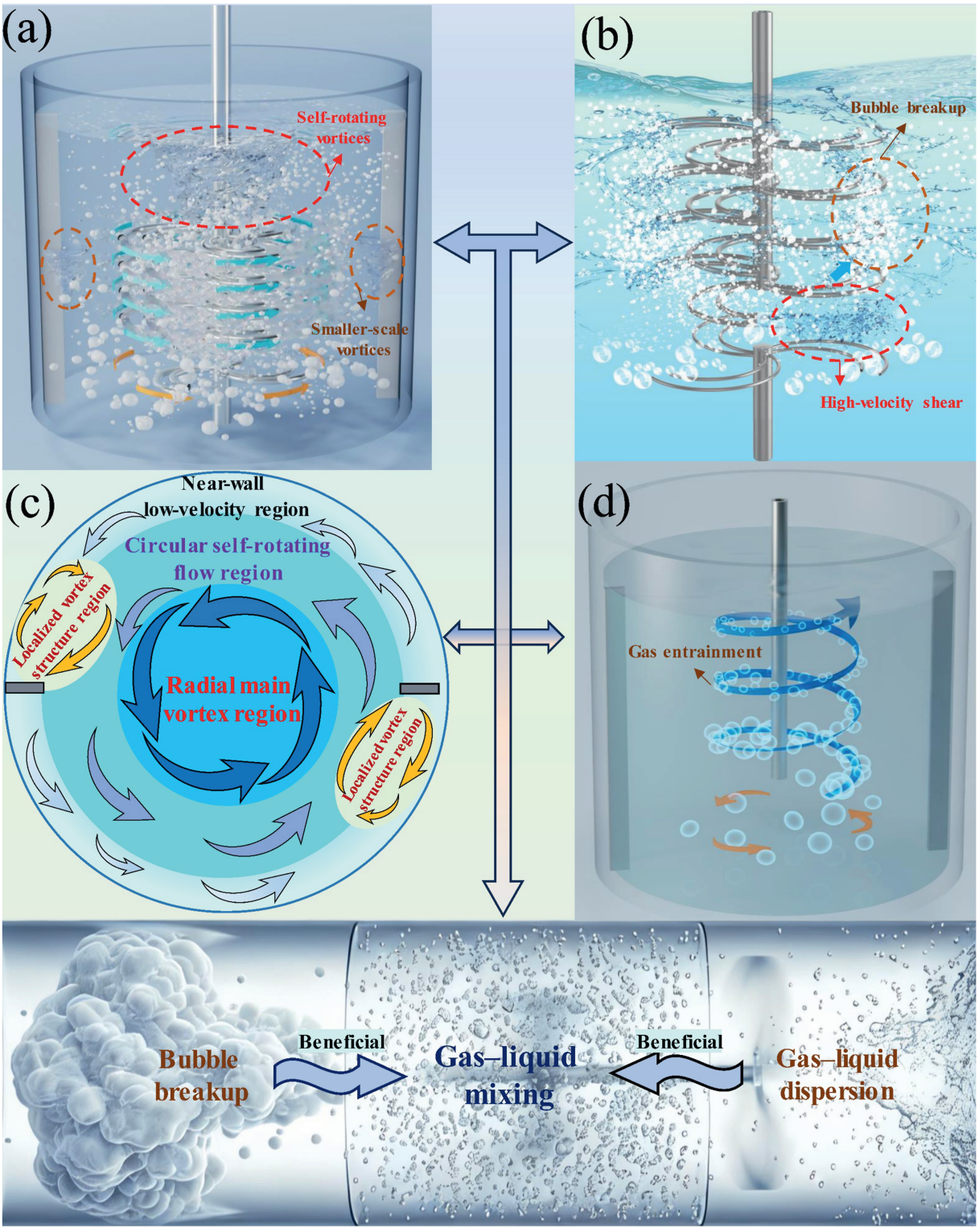


Fig. 19. Schematic representation of gas–liquid interaction mechanisms: (a) self-rotating vortices; (b) high-velocity shear effects; (c) multi-zone flow coupling; (d) gas–liquid interaction.

4. Conclusions

In this study, we developed a novel multi-nozzle, multi-layer self-rotating hydraulic agitator combined with a single-layer gas distributor and integrated them within the tank. Through experimental measurements and CFD simulations, we characterized the bubble distribution, gas–liquid mass transfer, and flow field in the system. Experimentally, the geometric features of the bubbles and the k_La value were quantified, and CFD simulations were conducted to characterize the internal flow field. Based on these investigations, the main conclusions are as follows.

1. Self-rotating vortices and strong shear forces promote bubble break-up and interfacial renewal. Increasing the superficial gas velocity and liquid circulation rate can further enhance the flow field disturbances, leading to improved gas–liquid mixing and mass transfer.
2. The counter-installed distributor, combined with the arrangement of two baffles, effectively optimized the bubble morphology and distribution, promoting gas dispersion and enhancing mass transfer performance.
3. The orientation of the distributor affects the k_La and bubble characteristics. Compared with the co-installed configuration, the counter-installed distributor increases k_La by 3%–11%, reduces the average bubble diameter by 4%–8%, and increases the average aspect ratio by 4%–5.5%.
4. Within the testing conditions of this study, the k_La under pulsed intake indicated a limited effect relative to continuous intake. Our subsequent work will focus on optimizing the pulse parameters, particularly the pulse duty cycle, to assess their influence on mass transfer performance.
5. Compared to traditional mechanical stirring tanks, the hydraulic stirring tank achieved 20%–45% higher k_La, reduced the average bubble diameter by 25%–40%, and increased the average aspect ratio by 7%–8%, highlighting its potential for intensifying multiphase systems.
6. Mechanistic analysis revealed that self-rotating vortices, high-velocity shear effects, multi-zone flow coupling, and gas-liquid interactions play crucial roles in enhancing the overall tank performance.

CRediT Authorship Contribution Statement

Denghan Luo: Writing – review & editing, Writing – original draft, Validation, Methodology, Investigation. Xiaopeng Chen: Writing – review & editing, Conceptualization. Zhongyao Zhang: Software, Methodology, Formal analysis. Yong Jin: Validation, Supervision. Jiezhen Liang: Resources, Conceptualization. Zhangfa Tong: Visualization, Funding acquisition. Linlin Wang: Writing – review & editing, Supervision, Project administration, Funding acquisition, Data curation.

Declaration of Competing Interest

The authors declare that they have no known competing financial interests or personal relationships that could have appeared to influence the work reported in this paper.

Acknowledgements

This work was supported by the National Natural Science Foundation of China (22368006), Guangxi Science and Technology Major Program (Guike AA23062019), and Guangxi Natural Science Foundation (2024GXNSFAA999185), Guangxi Key Laboratory of Petrochemical Resource Processing and Process Intensification Technology (2023Z002, 2024Z001).

Supplementary Material

Supplementary data to this article can be found online at https://doi.org/10.1016/j.cjche.2026.03.018.

Nomenclature

A	projection area of the bubble, mm^2
C_L	dissolved oxygen concentration at a given time, $mg \cdot L^{-1}$
C_0	initial dissolved oxygen concentration, $mg \cdot L^{-1}$
C^*	saturated dissolved oxygen concentration, $mg \cdot L^{-1}$
D	Rushton turbine diameter, m
D_i	duty cycle of the i-th pulse
d_{eq}	bubble equivalent diameter, mm
d_i	equivalent diameter of the i-th bubble, mm
d_{32}	Sauter mean diameter, mm
E	bubble aspect ratio
E_i	aspect ratio of the i-th bubble
$\overline{E}$	bubble deformation rate
g	gravitational acceleration, $m \cdot s^{-2}$
H_j	pump head under hydraulic stirring conditions, m
H_m	pump head under mechanical stirring conditions, m
k_La	volume oxygen mass transfer coefficient, s^{-1}
L_{major}	major axis length of the bubble contour-fitted ellipse, mm
L_{minor}	minor axis length of the bubble contour-fitted ellipse, mm
N	number of baffles
N_p	Rushton paddle power number
N_r	stirring speed, $r \cdot min^{-1}$
n	number of bubbles
n_i	frequency of the i-th bubble size occurring
P_j	hydraulic stirring power, W
P_m	mechanical stirring power, W
$P_{v,j}$	hydraulic stirring power per unit volume, $W \cdot m^{-3}$
$P_{v,m}$	mechanical stirring power per unit volume, $W \cdot m^{-3}$
p	pressure, Pa
Q_m	liquid circulation rate during mechanical stirring, $m^3 \cdot h^{-1}$
Q_v	liquid circulation rate during hydraulic stirring, $m^3 \cdot h^{-1}$
T_i	the i-th pulse cycle, s
$\boldsymbol{u}$	velocity, $m \cdot s^{-1}$
u_g	superficial gas velocity, $m \cdot s^{-1}$
V_j	working volume of the hydraulic stirring tank, m^3
V_m	working volume of the mechanical stirring tank, m^3
ρ	density, $kg \cdot m^{-3}$
μ	dynamic viscosity, mPa·s

References

[1] X.Y. Lan, X.G. Shi, C.X. Wang, Y.P. Zhao, J.S. Gao, C.M. Xu, Process intensification of multiphase flow and reaction system: Perspectives, *Chem. Eng. Process. Process Intensif.* 204 (2024) 109938.
[2] P.G. Bourguett-Rosas, M.A. Arenas-García, B. Vergara-Porras, C. Guerrero-Barajas, A. Ordaz, Intensification of multiphase systems with a jet-loop reactor: characterization of mass transfer, mixing time, drop oil size, and biomass growth, *J. Chem. Technol. Biotechnol.* 99 (3) (2024) 737–745.
[3] V. Cappello, C. Plais, C. Vial, F. Augier, Scale-up of aerated bioreactors: CFD validation and application to the enzyme production by Trichoderma reesei, *Chem. Eng. Sci.* 229 (2021) 116033.
[4] D.F. Ma, G.W. Wang, Y.G. Ma, C.Y. Zhu, X.Y. Tang, Hydrodynamics behavior and mass transfer performance of gas–liquid two-phase flow in the honeycomb fractal microreactor, *Chem. Eng. J.* 462 (2023) 142228.
[5] A. Yip, D. O'Malley, A. Meddaoui, J. Marton, D. Pjontek, J. Haelssig, Gas-liquid mass transfer and hydrodynamics in a vertically-oscillating multiphase reactor, *Chem. Eng. Sci.* 225 (2020) 115817.
[6] H.Q. Yang, L. Wang, S.B. Wang, Y.X. Zheng, H. Wang, Study on the mixing characteristics of multiphase in nonlinear blowing-stirring systems and experimental application, *Chem. Eng. Res. Des.* 215 (2025) 453–464.
[7] G. Nadal-Rey, D.D. McClure, J.M. Kavanagh, B. Cassells, S. Cornelissen, D.F. Fletcher, K.V. Gernaey, Computational fluid dynamics modelling of hydrodynamics, mixing and oxygen transfer in industrial bioreactors with Newtonian broths, *Biochem. Eng. J.* 177 (2022) 108265.
[8] A.Q. Li, Y. Yao, X. Zhang, Y.D. Wang, C.Y. Tao, Z.H. Liu, Asymmetric mixing in unbaffled stirred tank reactors: A mini-review, *Chin. J. Chem. Eng.* 87 (2025) 273–287.
[9] P. Satjaritanun, J.R. Regalbuto, J.A. Regalbuto, N. Tippayawong, S. Shimpalee, Mixing optimization with inward flow configuration contra-rotating impeller, baffle-free tank, *Alex. Eng. J.* 60 (4) (2021) 3759–3779.
[10] N. Qiao, S. Yue, J.P. Cheng, C.D. Wang, X.F. Wang, Y.F. Shi, J.B. Guo, D.Y. Yu, A gas distributor capable of multiple injection directions to improve the

gas–liquid dispersion performance in the airlift loop reactor, *Biochem. Eng. J.* 190 (2023) 108770.
[11] D.Y. Gu, C.S. Li, Y.H. Song, H. Xu, T. Yao, Investigation on the chaotic mixing mechanism of high-viscosity fluids with laminar flow in an irregular impeller stirred tank, *Ind. Eng. Chem. Res.* 64 (16) (2025) 8480–8491.
[12] B.Q. Liu, Q. Xiao, N. Sun, P.F. Gao, F.Y. Fan, B. Sunden, Effect of gas distributor on gas–liquid dispersion and mass transfer characteristics in stirred tank, *Chem. Eng. Res. Des.* 145 (2019) 314–322.
[13] Z.Y. Wu, T.H. Yu, Y. Zhu, J.J. Cai, F. Zhou, Y. Nie, Experimental and numerical study of droplet breakup in a jet mixer, *Chem. Eng. Sci.* 313 (2025) 121771.
[14] M. Opletal, P. Novotný, V. Linek, T. Moucha, M. Kordač, Gas suction and mass transfer in gas-liquid up-flow ejector loop reactors. Effect of nozzle and ejector geometry, *Chem. Eng. J.* 353 (2018) 436–452.
[15] H. Warmeling, A. Behr, A.J. Vorholt, Jet loop reactors as a versatile reactor set up — intensifying catalytic reactions: A review, *Chem. Eng. Sci.* 149 (2016) 229–248.
[16] X. Jia, H.L. Liao, Q.F. Hu, Y.H. He, Y.F. Wang, W.L. Niu, Optimization method of jet pump process parameters and experimental study on optimal parameter combinations, *Processes* 11 (10) (2023) 2841.
[17] Z.L. Huang, Y. Shuai, C.J. Ren, Y. Yang, J.Y. Sun, J.D. Wang, Y.R. Yang, Effects of internal structures on mass transfer performance of jet bubbling reactor, *Chem. Eng. Process. Process Intensif.* 175 (2022) 108936.
[18] L. Panariello, D. Macrí, V. Zito, R. Solimene, P. Salatino, P. Lettieri, M. Materazzi, Experimental and numerical analysis of jet penetration and gas evolution in a single-nozzle distributor fluidized bed, *Chem. Eng. J.* 437 (2022) 135391.
[19] M. Wu, H.Y. Song, X. Liang, N. Huang, X.B. Li, Generation of micro-nano bubbles by self-developed swirl-type micro-nano bubble generator, *Chem. Eng. Process. Process Intensif.* 181 (2022) 109136.
[20] Z.W. Yao, H.X. Xu, J. Li, T.S. Xu, Multi-objective optimization of stirring tank based on multiphase flow simulation, *Chem. Eng. Res. Des.* 189 (2023) 680–693.
[21] C.C. Yin, J.Z. He, Y.N. Xiong, Z.B. Zhang, X. Luo, Y. Shu, D.F. Long, K.H. Zheng, Improved suspension quality and liquid level stability in stirred tanks with Rotor-Stator agitator based on CFD simulation, *Particuology* 82 (2023) 64–75.
[22] M.C. Chen, C. Zhang, W. Yang, S.Y. Zhang, W.J. Huang, End-to-end bubble size distribution detection technique in dense bubbly flows based on you only look once architecture, *Sensors* 23 (14) (2023) 6582.
[23] Y.H. Fu, X. He, S. Wang, Y.M. Zhao, L. Dong, Z.Q. Chen, Study of bubble behavior in a gas–solid dense-phase fluidized bed based on deep learning, *Fuel* 357 (2024) 129889.
[24] X. Wang, M.H. Song, S.Q. Li, Y. Huang, Dynamic behaviors of bubble formation on submerged micro-capillary under constant flow conditions, *Powder Technol.* 417 (2023) 118258.
[25] R. Herrmann-Heber, S.F. Reinecke, U. Hampel, Dynamic aeration for improved oxygen mass transfer in the wastewater treatment process, *Chem. Eng. J.* 386 (2020) 122068.
[26] X.Y. Li, S.W. Xie, H.Z. Liu, J. Gan, Z. Jiang, L.Y. Wang, H.Y. Zhu, G.L. Li, H. Li, K.Q. Chen, Enhancing CO_2 capture efficiency: CFD investigation of gas–liquid self-suction reactor configurations, *Sep. Purif. Technol.* 360 (2025) 130979.
[27] C. Poelma, Measurement in opaque flows: A review of measurement techniques for dispersed multiphase flows, *Acta Mech.* 231 (6) (2020) 2089–2111.
[28] H.Z. Wang, X.X. Duan, X. Feng, D.W. Huang, W.J. Wu, W.P. Zhang, Z. Li, Y.F. Chen, C. Yang, Investigation of the gas–liquid–solid stirred tank by using the intrusive image-based method, *Ind. Eng. Chem. Res.* 62 (47) (2023) 20436–20448.
[29] W.F. Wu, M.L. Lian, S. Li, Coupled CFD-DEM simulation of fluids and bubbles in a stirring tank, *AIP Adv.* 15 (7) (2025) 075222.
[30] X.B. Zhang, Z.H. Luo, Local gas–liquid slip velocity distribution in bubble columns and its relationship with heat transfer, *AIChE J.* 67 (1) (2021) e17032.
[31] A.C. Dimian, A.A. Kiss, Novel energy efficient process for acetic acid production by methanol carbonylation, *Chem. Eng. Res. Des.* 159 (2020) 1–12.
[32] E.L. Paul, V.A. Atiemo-Obeng, S.M. Kresta, Handbook of Industrial Mixing: Science and Practice, Wiley, Hoboken, 2003.
[33] F. Maluta, F. Alberini, A. Paglianti, G. Montante, Hydrodynamics, power consumption and bubble size distribution in gas–liquid stirred tanks, *Chem. Eng. Res. Des.* 194 (2023) 582–596.
[34] H.Y. Bie, J.Z. He, K.X. Chen, L.C. Xue, G. Liu, Z.R. Hao, Study on the bubble breakup and internal flow characteristics in the pulsed jet ejector, *Chem. Eng. Process. Process Intensif.* 202 (2024) 109836.
[35] Z.Y. Zhang, L.F. Huang, H.Z. Xie, X.P. Chen, J.Z. Liang, X.J. Wei, C.H. Wu, L.L. Wang, New insights into relationship between gas cavities with operating conditions and hydrodynamic characteristics in aerated stirred tanks: Integrated *in-situ*/DIP/ROIMI/BIV quantization and CFD simulation, *Sep. Purif. Technol.* 340 (2024) 126706.
[36] C. Peng, Y.K. Liu, W.H. Gui, Z.H. Tang, Q. Chen, Bubble image segmentation based on a novel watershed algorithm with an optimized mark and edge constraint, *IEEE Trans. Instrum. Meas.* 71 (2022) 5005110.
[37] G.H. Chen, Z.C. Zhang, F. Gao, J.L. Li, J.P. Dong, Effect of different configurations on bubble cutting and process intensification in a micro-structured jet bubble column using digital image analysis, *Processes* 9 (12) (2021) 2220.
[38] Z.B. Song, J.H. Bi, X. Xu, Q. Yang, Pressure drop and gas holdup in an upward-flow fixed-bed reactor, *Chin. J. Chem. Eng.* 88 (2025) 42–52.
[39] L. Liu, H.Y. Zhang, H.J. Yan, T. Ziegenhein, H. Hessenkemper, P. Zhou, D. Lucas, Experimental studies on bubble aspect ratio and corresponding correlations under bubble swarm condition, *Chem. Eng. Sci.* 236 (2021) 116551.
[40] Y.N. Zhang, Z. Lu, Y. Qiao, K. Guo, W. Li, H. Liu, X. Li, C.J. Liu, Gas holdup, bubble size distribution, and mass transfer in an airlift reactor with ceramic membrane and perforated plate distributor, *Can. J. Chem. Eng.* 101 (11) (2023) 6613–6631.
[41] X. Xu, L. Wang, H.L. Wang, H.L. Liu, Q. Yang, Circulating jet for enhancing the mass transfer in a gas–liquid stirred tank reactor, *AIChE J.* 68 (1) (2022) e17392.
[42] L.A. Tribe, C.L. Briens, A. Margaritis, Determination of the volumetric mass transfer coefficient ($k_L a$) using the dynamic "gas out–gas in" method: Analysis of errors caused by dissolved oxygen probes, *Biotechnol. Bioeng.* 46 (4) (1995) 388–392.
[43] Z.Y. Zhang, Y.J. Wu, X.P. Chen, J.Z. Liang, Q.Y. Tan, C.H. Wu, B. Feng, D.H. Luo, L. L. Wang, Hydrodynamics, mixing performance and power consumption in horizontal millimeter-scale helical tube reactors: comprehensive experimental and numerical investigations across a wide range of centrifugal-to-gravitational acceleration ratio, *Chem. Eng. J.* 530 (2026) 173168.
[44] X.B. Zhang, X.Q. Wang, H. Chen, Z.H. Luo, An improved theoretical model for eddy-induced bubble breakup in turbulent flows, *AIChE J.* 71 (5) (2025) e18757.
[45] X.B. Zhang, Q. Zeng, X.Q. Wang, Z.H. Luo, A turbulence-induced coalescence model for fluid particle incorporating particle size effect across full energy spectrum, *AIChE J.* 72 (4) (2026) e70233.
[46] H. Yang, Z.J. Lu, L.K. Ma, W. Yin, B.J. Wang, Z.S. Bai, X.Y. Yang, Experimental and numerical investigations on micromixing performance of multi-orifice cross-flow jet mixers, *Chin. J. Chem. Eng.* 70 (2024) 63–72.
[47] M.H. Zhang, F.R. Bao, R.S. Li, Z.F. Geng, X.Y. Guan, H. Dong, Computational investigation on the flow and mass transfer properties inside ejector of loop reactor based on CFD-PBM simulation, *Powder Technol.* 428 (2023) 118869.
[48] P.J. Roache, Verification and Validation in Computational Science and Engineering, Hermosa Publ., Albuquerque, NM, 1998.
[49] J.H. Ferziger, M. Perić, R.L. Street, Computational Methods for Fluid Dynamics, fourth ed., Springer, Cham, 2020.
[50] X.L. Xing, C. Zhang, B. Jiang, Y.L. Sun, L.H. Zhang, C. Briens, Effect of a baffle on bubble distribution in a bubbling fluidized bed, *Processes* 9 (7) (2021) 1150.
[51] L.Y. Wang, Y.P. Wei, Z. Jiang, C. Hong, X.Y. Li, H.Z. Liu, Q. Hu, H. Li, G.L. Li, K.Q. Chen, Bubble size, mass transfer, and hydrodynamics in a self-priming aeration draft tube reactor, *Chem. Eng. Res. Des.* 219 (2025) 79–90.
[52] T. Lacassagne, M. EL Hajem, J.Y. Champagne, S. Simoëns, Turbulent mass transfer near gas–liquid interfaces in water and shear-thinning dilute polymer solution, *Int. J. Heat Mass Tran.* 194 (2022) 122975.
[53] S.P. Evgenidis, T.D. Karapantsios, Increase of gas–liquid interfacial area in bubbly flows by pulsating flow conditions, *Chem. Eng. J.* 486 (2024) 150107.
[54] Q. Zhang, Z.Y. Dong, Z.K. Liu, G.W. Chen, Effect of ultrasonic waveforms on gas–liquid mass transfer in microreactors, *AIChE J.* 68 (8) (2022) e17689.
[55] P.V. Danckwerts, Significance of liquid-film coefficients in gas absorption, *Ind. Eng. Chem.* 43 (6) (1951) 1460–1467.
[56] N. Afraz, A. Adi, K. Hecht, The effect of diffusion on mass transfer in a laminar falling film: Observation *versus* theory, *Chem. Eng. Sci.* 232 (2021) 116363.
[57] S.C. Kaiser, S. Werner, V. Jossen, M. Kraume, D. Eibl, Development of a method for reliable power input measurements in conventional and single-use stirred bioreactors at laboratory scale, *Eng. Life Sci.* 17 (5) (2017) 500–511.
[58] A.W. Nienow, On impeller circulation and mixing effectiveness in the turbulent flow regime, *Chem. Eng. Sci.* 52 (15) (1997) 2557–2565.
[59] T. Kracík, T. Moucha, R. Petříček, Gas–liquid contactors' aeration capacities when agitated by rushton turbines of various diameters, *ACS Omega* 5 (10) (2020) 5072–5077.
[60] C. Yang, J.X. Yao, X.H. Chen, M.H. Xie, G.Z. Zhou, Z.L. Xu, B.Q. Liu, Experimental study on gas–liquid flow regimes of coaxial mixers equipped with a Rushton/pitched blade turbine and anchor, *Chem. Eng. Res. Des.* 202 (2024) 377–389.
[61] R.H. Perry, D.W. Green, M.Z. Southard (Eds.), Perry's Chemical Engineers' Handbook, 8th ed., McGraw-Hill, New York, 2008.
[62] F. Alberini, A. Albano, P. Singh, C. Christodoulou, G. Montante, F. Maluta, A. Paglianti, Fluid dynamics and power consumptions in a single use stirred tank adopted in the pharmaceutical industry, *Chem. Eng. Res. Des.* 204 (2024) 159–171.
[63] M. Taghavi, R. Zadghaffari, J. Moghaddas, Y. Moghaddas, Experimental and CFD investigation of power consumption in a dual Rushton turbine stirred tank, *Chem. Eng. Res. Des.* 89 (3) (2011) 280–290.
[64] B.R. Wang, G.Q. Yang, H.Z. Tian, X.B. Li, G.D. Yang, Y.K. Shi, Z. Zhou, F. Zhang, Z. B. Zhang, A new model of bubble Sauter mean diameter in fine bubble-dominated columns, *Chem. Eng. J.* 393 (2020) 124673.
[65] Y.D. Liu, J.H. Guo, W.P. Li, W. Li, J.L. Zhang, Investigation of gas–liquid mass transfer and power consumption characteristics in jet-flow high shear mixers, *Chem. Eng. J.* 411 (2021) 128580.
[66] Y.Y. Dong, F.C. Qiu, X.J. Chai, CFD simulation investigation on the flow field distribution pattern under different operating environment pressures in a jet impingement-negative pressure reactor, *ACS Omega* 9 (1) (2024) 1925–1935.
[67] X. Dong, Y.R. Shan, C. Xue, Y.N. Liu, Y. Feng, J.W. Zhang, Bubble plume behavior and turbulence characteristics of gas–liquid phase in power-law fluids, *Chem. Eng. Technol.* 48 (1) (2025) e202400257.
[68] E.H. Cao, A.N.P. Radhakrishnan, R. bin Hasanudin, A. Gavriilidis, Study of liquid–solid mass transfer and hydrodynamics in micropacked bed with gas–liquid flow, *Ind. Eng. Chem. Res.* 60 (29) (2021) 10489–10501.